Elastic Mechanics Study of Layered Li(Ni$_x$Mn$_y$Co$_z$)O$_2$

Jiahua Liu, Weicheng Lin, Zhu Wang, Ying Wang, Taowen Chen, and Jiaxin Zheng[*]

School of Advanced Materials, Peking University Shenzhen Graduate School, Shenzhen 518055, China

Understanding the elastic mechanical behavior of layered Li(Ni$_x$Mn$_y$Co$_z$)O$_2$ (NMC) cathode materials is critical for developing strategies to address their prominent cracking issues and mitigate the mechanical degradation of the cathode of lithium-ion batteries (LIBs). So far, a systematic and in-depth investigation into the elastic mechanical properties of NMC materials is still lacking. Hence, both the isotropic and anisotropic mechanical properties, including elastic constants, Young's modulus, shear modulus, bulk modulus, compressive modulus, linear compressibility, Poisson's ratio, Pugh's ratio, Cauchy pressure, and Kube's log-Euclidean and universal elastic anisotropy indexes, of seven NMC materials with different compositions are systematically studied here through first-principles calculations. The bulk modulus is proved to be an isotropic mechanical quantity, and its proper relationship with the anisotropic linear compressibility is revealed. Then, we investigate how the isotropic and anisotropic mechanical properties of NMC materials can be tuned by the compositions of Ni, Mn, and Co. It is found that the elastic moduli of NMC materials decrease as the Ni content increases, and Mn plays a positive role in not only enhancing the elastic moduli but also in reducing the mechanical anisotropy of NMC materials. Through a quantitative chemical bond analysis, we find that the reason for such a dependence of the elastic moduli on the transition metal (TM) compositions of NMC materials lies in the difference in the strengths of TM–O bonds, and the positive effect of Mn mainly stems from the contribution of the ionic bonding part of the Mn−O bond due to the high average valence state (+4) of Mn ions; this highlights the benefits of doping with other high-valence-state ions for the promotion of the mechanical properties of NMC materials. Besides, the applicability, physical meaning, and proper use of Pugh's ratio and the Cauchy pressure in metal-oxides like NMC materials, as well as their relations with Poisson's ratio, are clarified. The analysis of the relative ductility and brittleness of NMC materials with different compositions via Pugh's ratio and the isotropic Poisson's ratio reveals a negative correlation between the relative ductility and the magnitude of the modulus. Cauchy pressures of layered NMC materials are found to be directional, with an intralayer negative value but an interlayer positive value, which predicts the significant covalent bonding character of the TM–O bonds, but a nearly ionic dominated bonding character of the Li−O bonds, and this qualitative result has been further proved by a quantitative chemical bond analysis. Furthermore, an in-depth investigation of the three-dimensional spatial distribution characteristics of anisotropic mechanical properties of NMC materials is conducted. It is found that, first, the distributions of directions of the extreme values of various anisotropic mechanical properties all exhibit an approximate trigonal symmetry to some extent; second, the anisotropy is most prominent in the {2$\bar{1}$0} crystal plane family; third, the (104) plane and [$\bar{4}\bar{8}$1] direction are, respectively, prone to be the cleavage plane and cleavage direction, along which the microcracks and even mechanical failures may be susceptible to occur due to stress concentration. The findings presented in this study will provide guidance for the design and development of robust and reliable LIBs.

*zhengjx@pkusz.edu.cn

I. INTRODUCTION

The rechargeable lithium-ion battery (LIB) has become a piece of equipment required daily for modern human society, as it plays a vital role in powering today's various portable electronics and electrical vehicles (EVs). The performance and durability of current LIBs are largely determined by the cathode materials, among which the layered Li(Ni$_x$Mn$_y$Co$_z$)O$_2$ (NMC, $x+y+z=1$)

materials have emerged as the frontrunners due to their high energy density [1–3]. To meet the increasing demands for longer driving ranges of EVs, NMC materials are gradually evolving towards a higher nickel content [1]. However, the Ni-rich NMC materials suffer from poor cycling stability caused by microcracking, owing to the high degree of lithium utilization [4–10]. Therefore, investigating the mechanical properties of layered NMC cathode materials is essential for developing strategies to mitigate mechanical degradation and improve the long-term cycling stability and reliability of LIBs.

Previous traditional polycrystalline NMC materials (PNMCs) consist of secondary particles formed by agglomerating primary particles, and the intergranular fracture and induced decohesion between primary grains constitute the major mechanical degradation processes in the weakly bonded NMC secondary particles [11–13]. Therefore, the so-called "single-crystal" NMC materials (SNMCs), directly comprised of microsized primary particles, were proposed and have been successfully applied in recent years due to their better structural integrity and stability under cycling compared with the PNMCs [14–21]. However, despite the effectively alleviated intergranular cracking in SNMCs, intragranular microcracking can still be observed within the single-crystalline particles of SNMCs after long-term cycling under high cutoff voltages [15,22–24]. In addition, besides intergranular cracking, intragranular cracking is also a prominent issue in PNMCs [25–27]. To address the issue of intragranular cracking, it is crucial to investigate the anisotropic mechanical properties within the primary single-crystalline particles of NMC materials because this knowledge holds important guiding significance for microscopic mechanical failure analysis of NMC materials. For instance, along the direction of the minimum value of the anisotropic Young's modulus, crystal cleavage is prone to occur due to stress concentration, leading to microcracks and even mechanical failures. As another example, the motion of dislocations is closely related to the magnitude of the shear modulus. Along the planes where the two directions of the minimum value of the anisotropic shear modulus are located, the resistance to dislocation motion is lower, making the crystal susceptible to slipping and resulting in plastic deformation. It has been reported that the motion of dislocations is closely related to the generation and propagation of intragranular cracks in layered NMC [25,27] and LiNiO$_2$ (LNO) [28] cathode materials. Additionally, recent studies have revealed a close correlation between the dislocation slipping and phase transitions during the delithiation process in layered LNO [28–30], LiCoO$_2$ (LCO) [30], and NMC [31] cathode materials. Therefore, investigating the anisotropic shear modulus of NMC materials is also helpful to understand their phase transition behavior. Additionally, the anisotropic elastic properties are also very important for studying the change of electrochemical potential due to stress at the solid-solid interfaces between the solid electrolyte and electrode, since previous works [32,33] have shown that the resistance to the formation of dendrites at the Li metal anode can be affected and tuned by different isotropic and especially anisotropic elastic properties. Therefore, such studies can also be conducted for the interfaces between the solid electrolyte and cathode materials such as NMC, if knowledge of the anisotropic elastic properties of the latter can be accessed.

Several previous works reported experimental measurements [12,34–37] or theoretical computations [38] of the mechanical properties of NMC materials. Nevertheless, these results involved only the isotropic mechanical properties, while the anisotropic elastic mechanical properties of NMC materials are rarely reported. On the one hand, the complete sets of elastic constants that characterize the entire mechanical anisotropy of a single crystal are hard to obtain experimentally due to the requirement for large (macroscopic sized) grain single crystals and the difficulty in precise experimental measurements, in particular for low-symmetry crystals like NMC materials. On the other hand, although elastic constants can be accessed by first-principles calculations, the computational cost and accuracy of the elastic calculation results are closely related to the symmetry of the crystal. Therefore, despite several reports [30,39,40] on the computational results of elastic constants and the anisotropic elastic properties of LCO and LNO with simple lattices, it is hard to find similar reports for NMC materials with a more complex lattice. In computational work by Sun and Zhao [38], the elastic constants of some NMC materials seem to have been calculated through the virtual crystal approximation [41,42] method, which is often used for alloy systems, but they only studied the isotropic mechanical properties obtained from the elastic constants, whereas the anisotropic mechanical properties were not investigated and the elastic constants were not provided in their paper. The elastic constants of Li(Ni$_{0.8}$Mn$_{0.1}$Co$_{0.1}$)O$_2$ were reported in the work of Li *et al.* [43], while the results are missing nonzero elements like C_{14}, and hence, are not a complete set of elastic constants. Very recently, Zhao's group [44] reported the experimental measurement results of the anisotropic mechanical properties of NMC materials, yet their measurement results had quite a large range of deviations, and the elastic constants were only available for Li(Ni$_{0.6}$Mn$_{0.2}$Co$_{0.2}$)O$_2$. Considering the fact that the mechanical properties are wildly different for NMC materials with different compositions of Ni, Mn, and Co, there is still a lack of systematic and in-depth research on the complete anisotropic mechanical properties based on precise elastic constants.

This paper aims to systematically and comprehensively study the elastic mechanical properties of various layered

NMC cathode materials through first-principles calculations. Both the isotropic mechanical properties, including the Young's modulus, shear modulus, bulk modulus, Poisson's ratio, and Pugh's ratio, and the anisotropic mechanical properties, including elastic constants, the Young's modulus, shear modulus, compressive modulus, linear compressibility, Poisson's ratio, and Cauchy pressure, are systematically studied for seven NMC materials with different compositions. The contents of this paper are primarily divided into two main sections: theory and computational results. In the theory section, we offer a brief overview of the fundamentals of elastic mechanics first, and then, considering the extensive errors present in the relevant literature, the proper methods of obtaining various isotropic and anisotropic mechanical properties and their interrelations are introduced. We place an emphasis on demonstrating that the bulk modulus is an isotropic mechanical quantity and discuss its proper relationship with the anisotropic linear compressibility or compressive modulus. Besides, the correct forms of Cauchy pressures for different crystal systems and their relations are clarified. In the section on the computational results, how the isotropic and anisotropic mechanical properties of NMC materials can be tuned by the compositions of Ni, Mn, and Co is investigated by contrasting their individual contributions. In addition, in response to the widespread misuse of the Pugh's ratio in numerous research papers, the applicability and correct usage of the Pugh's ratio in metal-oxides like NMC materials is clarified, and the relative ductility and brittleness of NMC materials with different compositions are analyzed via Pugh's ratio and the isotropic Poisson ratio. Furthermore, the three-dimensional (3D) spatial distribution characteristics of various anisotropic mechanical properties of NMC materials are studied by analyzing the directions of their extreme values. Besides, the elastic anisotropy within the three major crystallographic planes $(2\bar{1}0)$, (010), and (001), is investigated, and in particular, the relationships between the distribution directions of extreme values of the Young's modulus and the atomic packing direction in the $(2\bar{1}0)$ crystal plane with the most prominent anisotropy are revealed. Moreover, the overall elastic anisotropy of various NMC materials is examined by using the universal and Kube's log-Euclidean elastic anisotropy indexes. Additionally, the physical meaning of the Cauchy pressure, its relations with Pugh's ratio and Poisson's ratio, as well as its proper use, are elaborated. Then the qualitative bonding character of layered NMC materials is evaluated by the Cauchy pressure. Finally, quantitative chemical bond analysis is discussed to garner a deeper understanding of the mechanical properties of NMC materials.

II. COMPUTATIONAL METHODS

The first-principles calculations were implemented within the plane-wave-basis-set-based Vienna *ab initio*

simulation package (VASP) [45,46] under the Kohn-Sham-equation-based density functional theory (DFT) [47,48] framework. The Perdew-Burke-Ernzerhof [49,50] exchange-correlation functional at the generalized gradient approximation level was chosen. The projector augmented-wave method [51,52] was used to describe the interactions between the core and shell electrons. The Hubbard U approach [53,54] was adopted to correct the strong Coulomb repulsion between the partly filled valence $3d$ shell electrons localized on transition metal ions, and the U parameters were set as 6.4, 3.3, and 3.5 eV for Ni, Co, and Mn, respectively, according to our own tests in our previous studies [55,56], as they have shown good consistency with experimental data. To ensure the convergence of the stress tensor, which is crucial in elastic calculations by the stress-strain method, parameters including ENCUT, k-point density, EDIFF, and EDIFFG have been carefully tested. The results indicate that 700 eV is enough for the cutoff energy ENCUT of plane waves, and this is greater than the recommended value ("ENCUT $= 1.3 \times$ default cutoff" according to the VASP manual) and is also consistent with the previous study [57]. A uniform k-point density of approximately 1000 per reciprocal atom [57] is used by setting the KSPACING values according to the supercell size. The energy convergence criterion EDIFF for the electronic self-consistent loop is set to 10^{-7} eV in all our calculations to obtain very accurate results. The full geometry optimizations (which mean that all the degrees of freedom, including ionic positions, cell volume, and cell shape, are allowed to change) were performed by using the conjugate-gradient minimization approach and the calculations did not stop until the Hellmann-Feynman forces EDIFFG were less than 0.01 eV Å^{-1} per atom. In addition, the full geometry optimizations were repeatedly carried out by successively copying the CONTCAR to the POSCAR and restarting the run until the number of relax steps of the final relaxation calculation reduced to 1, which meant that the final full relaxation was a volume conserving relaxation which ensured elimination of the Pulay stress. All our calculations were carried out with spin polarization, and an antiferromagnetic structure [55,56,58–62] was adopted for all the NMC materials. All the supercell structures built in this work are based on the layered trigonal LiNiO$_2$ and LiCoO$_2$ structures with space group $R\bar{3}m$, as the prototype α-NaFeO$_2$ model. More details about the construction of supercell models are discussed in Sec. S1 within the Supplemental Material [63] (see also Refs. [64–74] therein).

III. THEORY

A. Basics of elastic theory

The generalized form of Hooke's law expressed by tensors can be written as [75]

$$\sigma_{ij} = C_{ijkl}\varepsilon_{kl}, \qquad (1)$$

where σ_{ij} and ε_{kl} are the second-rank stress tensor and strain tensor, respectively, each containing nine components. C_{ijkl} denotes the fourth-rank elastic stiffness tensor, which consists of 81 stiffness constants. Note the Einstein summation convention is adopted in Eq. (1). Considering the symmetry of the stress and strain tensors, the number of independent σ_{ij} and ε_{kl} components are both reduced from nine to six, which reduces the total number of independent C_{ijkl} constants from 81 to 36. Hence, Eq. (1) can be simplified from the tensor form to the following matrix form:

$$\sigma_i = \sum_{j=1}^{6} C_{ij}\varepsilon_j, \qquad (2)$$

by adopting the Voigt notation [75], i.e.,

$$\sigma_{xx} = \sigma_1, \quad \sigma_{yy} = \sigma_2, \quad \sigma_{zz} = \sigma_3,$$
$$\sigma_{yz} = \sigma_{zy} = \sigma_4, \quad \sigma_{xz} = \sigma_{zx} = \sigma_5, \quad \sigma_{xy} = \sigma_{yx} = \sigma_6, \qquad (3)$$

and

$$\varepsilon_{xx} = \varepsilon_1, \quad \varepsilon_{yy} = \varepsilon_2, \quad \varepsilon_{zz} = \varepsilon_3,$$
$$\varepsilon_{yz} + \varepsilon_{zy} = \varepsilon_4, \quad \varepsilon_{xz} + \varepsilon_{zx} = \varepsilon_5, \quad \varepsilon_{xy} + \varepsilon_{yx} = \varepsilon_6. \qquad (4)$$

Due to the arbitrariness of the order of the differential, C_{ij} in Eq. (2) is a symmetric matrix, which actually possesses only 21 independent stiffness constants, and thus, can be written as

$$C_{ij} = \begin{bmatrix} C_{11} & C_{12} & C_{13} & C_{14} & C_{15} & C_{16} \\ & C_{22} & C_{23} & C_{24} & C_{25} & C_{26} \\ & & C_{33} & C_{34} & C_{35} & C_{36} \\ & & & C_{44} & C_{45} & C_{46} \\ & & & & C_{55} & C_{56} \\ & & & & & C_{66} \end{bmatrix}. \qquad (5)$$

The above stiffness constants are calculated in VASP by the finite difference method, which performs six finite distortions on the lattice and then derives the elastic constants from the stress-strain relationship [76]. Furthermore, the ionic relaxation contributions are included by considering the displacements of each ion in each direction of Cartesian coordinates and then inverting the ionic Hessian matrix and multiplying by the internal strain tensor [77].

B. Isotropic mechanical properties

Based on the obtained stiffness constants C_{ij} from DFT calculations, isotropic polycrystalline mechanical properties can then be obtained by using some approximation methods. The most widely used approximation method is the Voigt-Reuss-Hill (VRH) approximation because it is simple, practical, and usually close to experimental values. Therefore, the VRH approximation is adopted in this work, and thus, a brief introduction to it is given below. Considering the random orientation of crystallites, a regular polycrystalline material may be treated as quasi-isotropic or isotropic in a statistical sense. The elastic response of an isotropic system is generally described by the bulk modulus, B, and shear modulus, G, which may be obtained by averaging the single-crystal elastic constants [78,79]. Voigt [80] proposed an averaging scheme to obtain the effective isotropic elastic modulus based on the assumption that the strain field is uniform throughout the samples, resulting in the following equations:

$$B_V = \frac{1}{9}[(C_{11} + C_{22} + C_{33}) + 2(C_{12} + C_{23} + C_{31})], \quad (6)$$

$$G_V = \frac{1}{15}[(C_{11} + C_{22} + C_{33}) - (C_{12} + C_{23} + C_{31}) + 3(C_{44} + C_{55} + C_{66})]. \qquad (7)$$

In contrast, Reuss [81] proposed a different averaging scheme based on the assumption that the stress field is uniform throughout the samples, resulting in the following formulas:

$$\frac{1}{B_R} = [(S_{11} + S_{22} + S_{33}) + 2(S_{12} + S_{23} + S_{31})], \quad (8)$$

$$\frac{1}{G_R} = \frac{1}{15}[4(S_{11} + S_{22} + S_{33}) - 4(S_{12} + S_{23} + S_{31}) + 3(C_{44} + C_{55} + C_{66})], \qquad (9)$$

where S_{ij} are the compliance constants, which can be obtained from the inverse matrix of the stiffness matrix C_{ij}. Hill [82] demonstrated that the Voigt and Reuss schemes actually provided the upper and lower bounds, respectively, and found that their arithmetic mean value provided a better approximation of the polycrystalline elastic modulus, which was often close to experimental data [83]. Hence, the VRH approximation is given by

$$B_H = \frac{B_V + B_R}{2}, \qquad (10)$$

$$G_H = \frac{G_V + G_R}{2}. \qquad (11)$$

With the bulk modulus, B, and the shear modulus, G, obtained from the VRH approximation, one can get the isotropic Young's modulus, E, and Poisson's ratio, ν, by

$$E = \frac{9BG}{3B + G}, \qquad (12)$$

$$\nu = \frac{3B - 2G}{2(3B + G)}. \qquad (13)$$

The ratio of the isotropic bulk modulus to the isotropic shear modulus is called Pugh's ratio, which is denoted here by R^P, i.e.,

$$R^P = \frac{B}{G}. \tag{14}$$

As early as 1954, Pugh [84] comparatively analyzed the ratios of B to G for various pure metals and found that pure metals with higher values of this ratio had good malleability. This ratio was called Pugh's ratio by later researchers and was widely used in a wide variety of material systems, such as alloys [85,86], metal oxides [87], quasicrystals and bulk metallic glasses [88], and various kinds of materials [57]. In fact, Pugh's ratio and Poisson's ratio are correlated with each other. According to Eqs. (13) and (14), we can get [84]

$$\nu = \frac{3B - 2G}{2(3B + G)} = \frac{3R^P - 2}{6R^P + 2}, \tag{15}$$

or

$$R^P = \frac{B}{G} = \frac{2 + 2\nu}{3 - 6\nu} = \frac{2(1 + \nu)}{3(1 - 2\nu)}. \tag{16}$$

Equation (16) shows that within the entire theoretical value range of the isotropic Poisson's ratio, ν, i.e., $-1 < \nu < 0.5$ [89], the Pugh's ratio, R^P, increases monotonically with ν. Hence, like the Pugh's ratio, R^P, the isotropic Poisson's ratio, ν, can also be used to evaluate the plasticity and brittleness of materials [84,89]. It was pointed out in some reports [40,83,87] that there was a critical criterion for Pugh's ratio, namely, $R^P = B/G = 1.75$, and the materials were considered either as plastic or brittle, depending on whether their Pugh's ratio was greater or less than 1.75. However, in the other reports [78,79,88], the ratio of G to B was defined as Pugh's ratio, which is the reciprocal of R^P defined here by Eq. (14), and thus, the critical value became $G/B = 1/1.75 = 0.57$. And in some other reports [85,86], the critical value was set as $G/B = 0.5$, which was probably approximated from 0.57, and thus, this results in $R^P = B/G = 1/0.5 = 2$. If R^P takes these two so-called critical values, it can be solved from Eq. (16) that the corresponding critical values for the isotropic Poisson's ratio are 0.26 and 0.286, respectively.

C. Anisotropic mechanical properties

The most significant feature of the mechanical properties of a single crystal is anisotropy, and many mechanical quantities, such as the Young's modulus, shear modulus, Poisson's ratio, and linear compressibility, show such anisotropic properties. Anisotropy means spatial dependence, and hence, such anisotropic properties of these mechanical quantities can be obtained by examining the spatial distribution of the values of these mechanical quantities in various directions in 3D space. This can be done by performing the coordinate transformation of the elastic tensor. Here, the anisotropic Young's modulus is taken as an example to display how to achieve this.

In the Cartesian coordinate system, $O(x, y, z)$, the Young's modulus along the direction of a certain axis, such as the x axis can be given by [75,90,91]

$$E = \frac{1}{S_{11}} = \frac{1}{S_{1111}}. \tag{17}$$

The Young's modulus along the other directions, except for the y and z axes, cannot be simply obtained directly from S_{ij} through Eq. (17). However, considering the coordinate transformation relationship of elastic compliance tensor S_{ijkl} [see Eqs. (S2) and (S4) within the Supplemental Material [63]], they can be obtained from the Young's modulus along the x' axis of a new coordinate system, $O(x', y', z')$, which is determined by rotating the original coordinate system, $O(x, y, z)$, by a certain angle in 3D space [75,79,92]:

$$E' = \frac{1}{S'_{11}} = \frac{1}{S'_{1111}} = \frac{1}{r_{1i}r_{1j}r_{1k}r_{1l}S_{ijkl}} = \frac{1}{a_i a_j a_k a_l S_{ijkl}}. \tag{18}$$

Here, the Einstein summation convention is adopted. r_{ij} is the rotation matrix [i.e., the direction cosine matrix given by Eq. (S7) within the Supplemental Material [63]] of the coordinate axes between the two coordinate systems, and a_i is the direction cosine of the first axis basis vector, $\mathbf{a} = \mathbf{e}'_1$, of $O(x', y', z')$ in $O(x, y, z)$. More details about the coordinate transformation of the elastic tensor and the direction cosine matrix can be found in Sec. S2 within the Supplemental Material [63].

When the rotation angle takes different values, the direction of the x' axis can coincide with every orientation in 3D space, and hence, Eq. (18) can give the anisotropic Young's modulus along an arbitrary direction. The Young's modulus, E', expressed by Eq. (18) can be called the directional Young's modulus, which reveals that the anisotropic Young's modulus of a single crystal is a function of the direction cosine, a_i, of a certain vector, $\mathbf{a}$, in 3D space.

Similarly, the directional shear modulus, G'; directional Poisson's ratio, ν'; and directional linear compressibility, β', can be obtained by the following expressions, respectively [75,79,90–92]:

$$G' = \frac{1}{S'_{66}} = \frac{1}{4S'_{1212}} = \frac{1}{4} \frac{1}{r_{1i}r_{2j}r_{1k}r_{2l}S_{ijkl}}$$
$$= \frac{1}{4} \frac{1}{a_i b_j a_k b_l S_{ijkl}}, \tag{19}$$

$$\nu' = -\frac{S'_{12}}{S'_{11}} = -\frac{S'_{1122}}{S'_{1111}} = -\frac{r_{1i}r_{1j}r_{2k}r_{2l}S_{ijkl}}{r_{1i}r_{1j}r_{1k}r_{1l}S_{ijkl}}$$
$$= -\frac{a_i a_j b_k b_l S_{ijkl}}{a_i a_j a_k a_l S_{ijkl}}, \tag{20}$$

$$\beta' = S'_{11pp} = r_{1i}r_{1j}r_{pk}r_{pk}S_{ijkk} = r_{1i}r_{1j}S_{ijkk} = a_i a_j S_{ijkk}. \tag{21}$$

Unlike the Young's modulus, which can be determined in one direction, the determination of the shear modulus and Poisson's ratio requires two orthogonal directions. Hence, the direction cosine, b_j, of the second axis basis vector, $\mathbf{b} = \mathbf{e}'_2$, of $O(x', y', z')$ in $O(x, y, z)$ appears in Eqs. (19) and (20).

What should be clarified is that the bulk modulus is not an anisotropic mechanical quantity, which can be verified by [75]

$$B' = \frac{1}{S'_{mmpp}} = \frac{1}{r_{mi}r_{mi}r_{pk}r_{pk}S_{iikk}} = \frac{1}{S_{iikk}} = B. \tag{22}$$

In the summation process of the subscripts i in Eq. (22), $r_{mi}r_{mi}$ in each term of summation represents the inner product of the vector r_{mi} with itself. Here, r_{mi} for a certain i represents the ith column vector of the rotation matrix r_{ij}. (For example, r_{m1} represents the first column vector of rotation matrix r_{ij}.) Therefore, vector r_{mi} is a unit vector because the rotation matrix r_{ij} is an orthogonal matrix [see Eq. (S7) within the Supplemental Material [63]]. Hence, the result of the inner product of a unit vector r_{mi} with itself is naturally equal to one. For the same reason, $r_{pk}r_{pk}$ in Eqs. (21) and (22) represents the inner product of a unit vector r_{pk} with itself, and hence, the result is also equal to one in the summation process of the subscript k.

Owing to the similarity between the concepts of the bulk modulus and linear compressibility, which are both defined under the same precondition, i.e., the subjection to unit hydrostatic pressure, the bulk modulus is often mistaken for being equal to the reciprocal of the linear compressibility [79] or one-third of the reciprocal of the linear compressibility [93]. It is easy to find the resulting problem of the first wrong approach because directly setting $B = 1/\beta$ will cause the value of bulk modulus B to be obviously too large (much larger than both the Young's modulus and shear modulus). As for the second misleading approach, i.e., setting $B = 1/(3\beta)$, the result makes sense in value only for the cubic crystal system and isotropic materials, of which the linear compressibilities, β, along three coordinate axes are equal to each other (i.e., $S_{11kk} = S_{22kk} = S_{33kk}$), but it still does not make sense in concept; besides, it does not make sense in either value or concept for the other six crystal systems because their linear compressibilities, β, along three coordinate axes are not equal to each other (i.e., $S_{11kk} \neq S_{22kk} \neq S_{33kk}$). In fact, the reciprocal of linear compressibility is the concept of

the compressive modulus, which is an anisotropic mechanical quantity. Here, the compressive modulus is termed κ and, according to Eq. (21), the directional compressive modulus, κ', can be expressed as

$$\kappa' = \frac{1}{\beta'} = \frac{1}{S'_{11pp}} = \frac{1}{r_{1i}r_{1j}r_{pk}r_{pk}S_{ijkk}} = \frac{1}{r_{1i}r_{1j}S_{ijkk}}$$
$$= \frac{1}{a_i a_j S_{ijkk}}. \tag{23}$$

The elastic anisotropy of a crystal with arbitrary symmetry can be described by the universal anisotropy index, A^U, which is defined as [94]

$$A^U = \frac{B_V}{B_R} + 5\frac{G_V}{G_R} - 6 \geq 0, \tag{24}$$

where B_V and G_V are the bulk modulus and shear modulus in the Voigt approximation, as defined in Eqs. (6) and (7), respectively, and B_R and G_R are the bulk modulus and shear modulus in the Reuss approximation, as defined in Eqs. (8) and (9), respectively. The universal anisotropy index, A^U, is identically defined as equal to zero for locally isotropic single crystals, and any positive departure of A^U from zero indicates the extent of single-crystal anisotropy [94]. However, A^U is still a relative measure of anisotropy with respect to the limiting value (i.e., zero), and the magnitude of A^U cannot be used to compare the multiplicative relationship of anisotropy between two crystals [83,95]. To overcome this limitation, the log-Euclidean anisotropy index, A^L, was devised by Kube [95] through seeking an anisotropy distance measure between the Voigt and Reuss estimations of elastic constants; this is defined as [95]

$$A^L = \sqrt{\left[\ln\left(\frac{B_V}{B_R}\right)\right]^2 + 5\left[\ln\left(\frac{G_V}{G_R}\right)\right]^2}. \tag{25}$$

In contrast to A^U, which can provide only a relative measure of anisotropy, A^L, which is improved based on A^U, can provide an absolute measure of anisotropy for different crystals, and thus, is capable of comparing the multiplicative relationship between two crystals [95]. It is evident that $A^L \geq 0$; $A^L = 0$ denotes elastic isotropy, and any positive value of A^L indicates elastic anisotropy.

It may be a little confusing that A^U and A^L evidently have to be taken into account for both the bulk and shear contributions, but the bulk modulus is proved to be an isotropic mechanical quantity in Eq. (22). In fact, it should be noted that the bulk modulus defined in Eq. (22) is equal to the bulk modulus of the Reuss approximation given in

Eq. (8), i.e.,

$$B = \frac{1}{S_{iikk}} = \frac{1}{(S_{11} + S_{22} + S_{33}) + 2(S_{12} + S_{23} + S_{31})}$$
$$= B_R. \quad (26)$$

This fact again proves that the bulk modulus defined in Eq. (22) is an isotropic mechanical quantity because the Reuss approximation is an isotropic result. Actually, considering that the Voigt approximation and Reuss approximation are based on the two assumptions of a uniform distribution of strain field and a uniform distribution of stress field, respectively, it is not difficult to understand that the discrepancy between them can reflect the mechanical anisotropy of a crystal.

D. Cauchy pressure

The Cauchy pressure is widely used to predict the bonding characters of crystals. However, it is often misused, and the main mistake lies in directly extending the relational expression $C_{12} - C_{44}$, which is only applicable to the cubic crystal system, to other crystal systems with lower symmetry. For example, $C_{12} - C_{44}$ has been misused for hexagonal or trigonal crystals in some papers [96–99]; in addition, in some other papers [78,83,88], $C_{12} - C_{44}$ has been introduced as a universal rule by mistake, without emphasizing the limitation of its applicability only to the cubic crystal system. This mistake might stem from the fact that early research concerning the Cauchy pressure, such as Pettifor's article [100] published in 1992, mainly focused on cubic crystal metals; later, numerous papers [85,86,88,101–104] attributed the Cauchy pressure to Pettifor's 1992 article [100] as the source literature. Additionally, in the paper by Thompson and Clegg [105], it was even wrongly believed that the Cauchy pressure was defined by Pettifor. In fact, the Cauchy pressure stems from Cauchy relations and, according to the claim by Ledbetter and Migliori [106], the latter were reported as early as 1828; in addition, the term "Cauchy pressure" was reported [107–109] before Pettifor's 1992 article and was not defined by Pettifor. According to Haussühl [110], the complete Cauchy relations can be expressed as

$$C_{iijk} = C_{ijik}(i \neq j, k). \quad (27)$$

Equation (27) includes the following six relationships:

$$C_{1122} = C_{1212}, C_{1133} = C_{1313}, C_{2233} = C_{2323}, \quad (28)$$
$$C_{1123} = C_{1213}, C_{2213} = C_{2123}, C_{3312} = C_{3132}. \quad (29)$$

Equations (28) and (29) in tensor notation are consistent with the form in Voigt notation reported by Quesnel *et al.* [111]. Cauchy pressures are defined as the deviations from

these Cauchy relationships [112], and usually, only the three relationships in Eq. (28) are of concern, since they are related to the shear elastic constants, i.e., C_{1212}, C_{1313}, and C_{2323}. Hence, the three Cauchy pressures are (transformed from tensor notation to Voigt notation)

$$P_{xy}^{\mathrm{Cauchy}} = C_{12} - C_{66}, P_{yz}^{\mathrm{Cauchy}} = C_{23} - C_{44},$$
$$P_{zx}^{\mathrm{Cauchy}} = C_{13} - C_{55}. \quad (30)$$

Obviously, Eq. (30) is adapted for crystals with orthorhombic symmetry. For hexagonal, trigonal, and tetragonal crystal systems, owing to $C_{44} = C_{55}$ and $C_{13} = C_{23}$, Eq. (30) becomes

$$P_{xy}^{\mathrm{Cauchy}} = C_{12} - C_{66}, P_{yz}^{\mathrm{Cauchy}} = P_{zx}^{\mathrm{Cauchy}} = C_{13} - C_{44}, \quad (31)$$

and for the cubic crystal system, owing to $C_{44} = C_{55} = C_{66}$ and $C_{12} = C_{13} = C_{23}$, Eq. (30) becomes

$$P_{xy}^{\mathrm{Cauchy}} = P_{yz}^{\mathrm{Cauchy}} = P_{zx}^{\mathrm{Cauchy}} = C_{12} - C_{44}. \quad (32)$$

In fact, aside from widespread reports on the Cauchy pressure for cubic crystals, as expressed by Eq. (32), the Cauchy pressures, as expressed by Eq. (31), have been reported for hexagonal [113–118], trigonal [119,120], and tetragonal [115,117,121,122] crystal systems in the literature, and the Cauchy pressures, as expressed by Eq. (30), have also been reported for orthorhombic crystals in the literature [79,112,118,122–128].

IV. RESULTS AND DISCUSSION

A. Lattice parameters and volume

As shown in Fig. 1(a), the Li(Ni$_x$Mn$_y$Co$_z$)O$_2$ materials studied here include three representatives of the "Ni = Mn" group with the pure Ni^{2+} state [55,56,58], i.e., Li(Ni$_{0.33}$Mn$_{0.33}$Co$_{0.33}$)O$_2$ (NMC333), Li(Ni$_{0.4}$Mn$_{0.4}$Co$_{0.2}$)O$_2$ (NMC442), and Li(Ni$_{0.425}$Mn$_{0.425}$Co$_{0.15}$)O$_2$ (NMC552), and four representatives of the "Ni-rich" group with mixed Ni^{2+} and Ni^{3+} valence states [55,56,58], i.e., Li(Ni$_{0.5}$Mn$_{0.3}$Co$_{0.2}$)O$_2$ (NMC532), Li(Ni$_{0.6}$Mn$_{0.2}$Co$_{0.2}$)O$_2$ (NMC622), Li(Ni$_{0.7}$Mn$_{0.15}$Co$_{0.15}$)O$_2$ (NMC71515), and Li(Ni$_{0.8}$Mn$_{0.1}$Co$_{0.1}$)O$_2$ (NMC811). The supercell model of the NMC532 sample was selected as a representative, as shown in Fig. 1(c), which displayed a $R\bar{3}m$-like structure with some Ni atoms substituted by Mn and Co atoms from the prototype trigonal LNO lattice. However, as the symmetry of the lattice is significant for the calculation of the elastic tensor, here we emphasize that the substitution of partial transition metal (TM) atoms and its subsequent effect of lattice distortion will obviously reduce the symmetry of the lattice, causing the entire crystal to lose the trigonal symmetry of the original $R\bar{3}m$ lattice. Therefore,
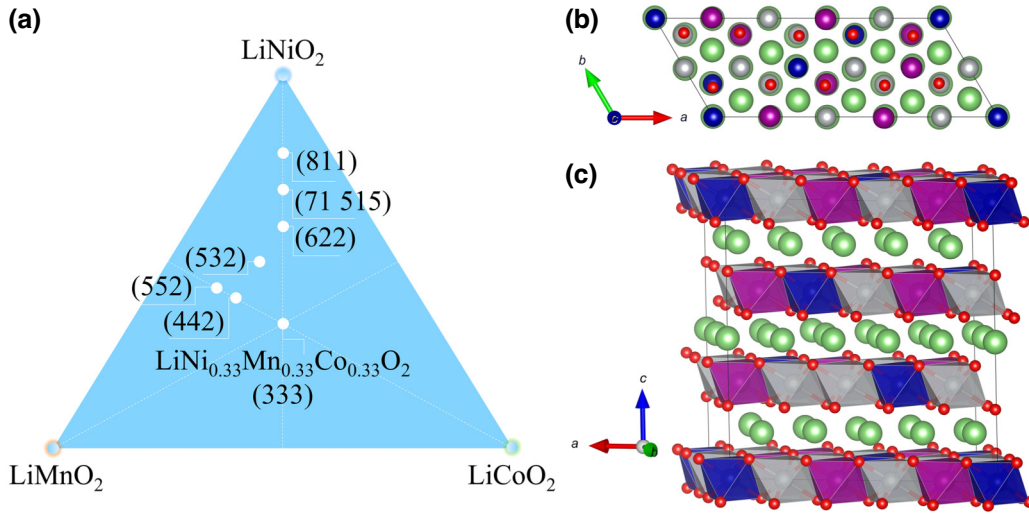
FIG. 1. (a) Schematic representation of the composition distribution of various NMC materials studied in this work. (b) Top view and (c) side view (visualized by VESTA [129]) of the crystal structure model for the supercell of $Li(Ni_{0.5}Mn_{0.3}Co_{0.2})O_2$ as a representative of the various NMC materials studied. Green, Li; red, O; silver, Ni; purple, Mn; blue, Co. Note that for the convenience of viewing, the relative size of O ions and metal ions shown here are not consistent with their actual sizes.

none of the NMC materials belongs to the $R\bar{3}m$ space group in the strict sense, and usually, they all directly become the lattice belonging to the $P1$ space group with the lowest symmetry (except for some individual cases with a superlattice arrangement of TM atoms).

The lattice constants and volume are significant for the calculation of mechanical properties, since the accuracy of the latter is very sensitive to the former. The calculated results of lattice constants a and c and volume V of the studied NMC materials are listed in Table S2 within the Supplemental Material [63] (see also Ref. [130] therein), in which the corresponding experimental results reported previously in the literature are also listed for the convenience of comparison. Our results show that the lattice constants a and c and volume V of various NMC materials calculated in this work are very close to their corresponding experimental values, with an average deviation between the calculated and experimental values of around 1% for lattice constants a and c and 2% for lattice volume V. The accuracy of these calculated results of lattice parameters provides a prerequisite for the accuracy of the subsequent calculated results of mechanical properties.

B. Elastic stiffness constant matrix and elastic stability

The calculated elastic stiffness constants, C_{ij}, of various NMC layered materials are listed in Table I. In addition, the C_{ij} of LNO with a standard $R\bar{3}m$ structure have also been calculated, and the results, as well as the standard template of C_{ij} of trigonal system I, are also listed in Table I for comparison. A more detailed explanation of

these matrices in Table I can be found in Sec. S3 within the Supplemental Material [63] (see also Ref. [131] therein). These elastic constants, which are not available in previous reports, are the most basic elastic properties and can be provided as the key prerequisite in subsequent more macroscopic simulations, such as finite element method calculations [43]. The specific form of the elastic constant matrix is closely related to the symmetry of the crystal because the latter can reduce the number of independent elastic constants. The triclinic crystal system with the lowest symmetry has 21 independent elastic constants [see Eq. (5)], while the $R\bar{3}m$ structure belonging to the trigonal crystal system has only six independent elastic constants (see Table I). Our calculated results (see Table I) demonstrate that the matrix C_{ij} of various NMC materials does not strictly, but only roughly, conform to the form of the template of C_{ij} of the $R\bar{3}m$ structure (although that of LNO does), which is consistent with what we mention above, namely, that no NMC materials belong to the $R\bar{3}m$ space group in the strict sense due to the reduced symmetry of the lattice caused by the partial substitution of TM atoms and the subsequent effect of lattice distortion. Nevertheless, it can be seen that, although the matrix C_{ij} of various NMC materials seems to resemble Eq. (5) of the triclinic crystal system, there are still many similar characteristics between the matrix C_{ij} of various NMC materials and that of LNO with the $R\bar{3}m$ structure. For example, for all the NMC materials, the following approximate relations between the elements of matrix C_{ij} are satisfied:

$$C_{11} \approx C_{22} \gg C_{33}, \qquad (33)$$

TABLE I. Calculated elastic stiffness constant matrix, C_{ij}, of various NMC layered materials in comparison with $R\bar{3}m$ LNO and the standard template of C_{ij} of the trigonal system I. Numbers in the positions corresponding to the non-zero matrix elements of the trigonal system I are highlighted in bold for the sake of comparison.

NMC	Elastic stiffness constants matrix C_{ij} (GPa)
$[C_{ij}]_{\text{trigonal I}}$	$\begin{bmatrix} C_{11} & C_{12} & C_{13} & C_{14} & 0 & 0 \\ & C_{11} & C_{13} & -C_{14} & 0 & 0 \\ & & C_{33} & 0 & 0 & 0 \\ & & & C_{44} & 0 & 0 \\ & & & & C_{44} & C_{14} \\ & & & & & \dfrac{C_{11}-C_{12}}{2} \end{bmatrix}$
LNO	$\begin{bmatrix} \mathbf{238.87} & \mathbf{86.22} & \mathbf{53.20} & \mathbf{-17.33} & 0 & 0 \\ & \mathbf{238.87} & \mathbf{53.20} & \mathbf{17.33} & 0 & 0 \\ & & \mathbf{192.03} & 0 & 0 & 0 \\ & & & \mathbf{40.95} & 0 & 0 \\ & & & & \mathbf{40.94} & \mathbf{-17.32} \\ & & & & & \mathbf{76.32} \end{bmatrix}$
333	$\begin{bmatrix} \mathbf{301.93} & \mathbf{87.72} & \mathbf{52.19} & \mathbf{-11.25} & 0.70 & 0.57 \\ & \mathbf{301.41} & \mathbf{51.61} & \mathbf{11.69} & -0.18 & -1.53 \\ & & \mathbf{216.28} & 0.12 & 0.23 & 0.30 \\ & & & \mathbf{49.72} & 1.27 & 0.40 \\ & & & & \mathbf{52.34} & \mathbf{-10.47} \\ & & & & & \mathbf{107.74} \end{bmatrix}$
442	$\begin{bmatrix} \mathbf{285.23} & \mathbf{83.84} & \mathbf{49.53} & \mathbf{-16.12} & -3.93 & -1.04 \\ & \mathbf{283.61} & \mathbf{49.49} & \mathbf{14.53} & -1.02 & -2.59 \\ & & \mathbf{206.62} & 1.96 & -0.34 & 0.16 \\ & & & \mathbf{45.15} & -1.48 & -0.94 \\ & & & & \mathbf{43.66} & \mathbf{-15.40} \\ & & & & & \mathbf{100.98} \end{bmatrix}$
552	$\begin{bmatrix} \mathbf{291.17} & \mathbf{85.01} & \mathbf{48.72} & \mathbf{-13.24} & -0.17 & 0.29 \\ & \mathbf{290.43} & \mathbf{48.51} & \mathbf{13.73} & -0.71 & -2.16 \\ & & \mathbf{208.85} & -0.08 & 0.69 & -0.04 \\ & & & \mathbf{48.33} & -0.61 & 0.46 \\ & & & & \mathbf{47.98} & \mathbf{-13.67} \\ & & & & & \mathbf{102.96} \end{bmatrix}$
532	$\begin{bmatrix} \mathbf{269.77} & \mathbf{81.45} & \mathbf{44.70} & \mathbf{-15.69} & 2.94 & 1.14 \\ & \mathbf{275.38} & \mathbf{44.69} & \mathbf{15.17} & 2.71 & 3.51 \\ & & \mathbf{197.77} & 0.54 & -0.95 & -0.09 \\ & & & \mathbf{44.44} & 0.65 & -0.57 \\ & & & & \mathbf{42.59} & \mathbf{-16.05} \\ & & & & & \mathbf{98.39} \end{bmatrix}$
622	$\begin{bmatrix} \mathbf{259.73} & \mathbf{84.15} & \mathbf{46.33} & \mathbf{-16.17} & -4.66 & -4.11 \\ & \mathbf{258.70} & \mathbf{46.44} & \mathbf{16.51} & 2.32 & 0.22 \\ & & \mathbf{198.41} & 0.79 & -2.17 & -1.33 \\ & & & \mathbf{44.93} & -2.26 & -1.47 \\ & & & & \mathbf{45.22} & \mathbf{-14.15} \\ & & & & & \mathbf{94.19} \end{bmatrix}$
71 515	$\begin{bmatrix} \mathbf{255.45} & \mathbf{81.79} & \mathbf{44.37} & \mathbf{-17.06} & -0.81 & -0.38 \\ & \mathbf{259.18} & \mathbf{45.63} & \mathbf{14.11} & -2.89 & -4.80 \\ & & \mathbf{193.67} & -1.59 & -1.73 & -1.07 \\ & & & \mathbf{43.40} & 0.08 & 0.56 \\ & & & & \mathbf{42.46} & \mathbf{-15.38} \\ & & & & & \mathbf{85.42} \end{bmatrix}$
811	$\begin{bmatrix} \mathbf{245.19} & \mathbf{79.36} & \mathbf{42.43} & \mathbf{-16.58} & 0.64 & 0.80 \\ & \mathbf{262.52} & \mathbf{46.02} & \mathbf{10.86} & -0.25 & 0.47 \\ & & \mathbf{196.89} & -2.70 & 0.90 & -0.65 \\ & & & \mathbf{46.80} & 0.51 & 0.99 \\ & & & & \mathbf{44.33} & \mathbf{-13.68} \\ & & & & & \mathbf{90.29} \end{bmatrix}$

$$C_{66} \approx \frac{C_{11} - C_{12}}{2} \gg C_{44} \approx C_{55}, \tag{34}$$

$$C_{13} \approx C_{23}, \tag{35}$$

$$C_{14} \approx -C_{15} \approx C_{56}, \tag{36}$$

$$C_{34} \approx C_{i5} \approx C_{i6} \approx 0 \ (i = 1, 2, 3, 4). \tag{37}$$

If all the approximately equal signs in the above relational expressions are replaced by equal signs, this corresponds to the case of $R\bar{3}m$ LNO. Therefore, the difference between the two sides of the approximately equal signs in the above relational expressions can be used as a method to evaluate the deviation of the symmetry of each NMC material from the trigonal crystal system. In fact, the relationships shown in Eqs. (33) and (34) reflect the characteristics of the anisotropic structure of layered materials, that is, the intralayer interaction is stronger than the interlayer interaction. Because the high stiffnesses of $C_{11} \approx C_{22}$ and C_{66} correspond to deformations (tensile and shear, respectively) within the layers where the bonding is strong, the low stiffnesses of C_{33} and $C_{44} \approx C_{55}$ correspond to deformations (tensile and shear, respectively) with components acting out of the layers where the bonding is relatively weak [132]. Here, strong intralayer bonding refers to the TM–O bonds within the TMO$_6$ slab [Fig. 1(c)], while weak interlayer bonding stands for the Li−O bonds between the two TMO$_6$ slabs [Fig. 1(c)]; this is further demonstrated through a quantitative chemical bond analysis in the following section.

Elastic stability is one of the important aspects of the reflection of lattice stability [133]. The most commonly used elastic stability criterion is to evaluate whether all the eigenvalues of a matrix C_{ij} are positive. The eigenvalues of the matrix C_{ij} of all our calculated NMC materials are positive, as can be seen from Table S3 within the Supplemental Material [63], which demonstrates that all our calculated NMC materials are elastically stable, and hence, reflects the reliability of our calculations. More details about the elastic stability assessment can be found in Sec. S4 within the Supplemental Material [63] (see also Refs. [134–136] therein).

C. Isotropic mechanical properties of polycrystalline NMC materials

The isotropic mechanical properties are of great significance to NMC cathode materials because both the recently popular SNMCs and the traditional PNMCs actually are polycrystalline materials. Through the previously introduced VRH approximation, the isotropic mechanical properties of various NMC materials can be obtained according to Eqs. (6)–(13). The results of these mechanical properties in the Voigt, Reuss, and Hill approximations, respectively, are depicted in Fig. 2, and the specific values of the Hill approximation results are listed in Table S4 within the

Supplemental Material [63], in which some previously reported experimental or computational results with specific numerical values [12,34,36,37] have also been listed. It can be seen that our results are generally consistent with the previously reported results, which mainly focus on the Young's moduli of NMC333 and NMC532 (Table S4 within the Supplemental Material [63]). In addition, there are still some other previously reported experimental [35] or computational [38] results that are not given as specific values but mentioned only in a range of values or just shown in diagrams in the original literature, and hence, those results are not listed in Table S4 within the Supplemental Material [63]. The estimated values of those results also show a general consistency with our data. In general, the values of previously reported experimental results are over a wide range, depending on different particle structures of samples and different testing methods. In fact, the results of DFT calculations for Young's moduli are closer to the experimental results of the densified NMC cathode samples rather than the usual NMC cathode with a porous secondary particle structure, as already shown in previous reports [12] and demonstrated here again in Table S4 within the Supplemental Material [63]. Therefore, only those experimental results [12,37] of the densified NMC cathode samples are displayed in Fig. 2 for the sake of clarity. As can be seen from Fig. 2, our calculated results show that the Voigt and Reuss approximations indeed provide the upper and lower bounds, respectively, and the Hill approximation, as their average, is naturally in the middle; this verifies the reliability of our DFT computational results of stiffness constants C_{ij}. More importantly, Fig. 2 shows that, among the three approximation results, the Hill approximation results are indeed closer to, and actually very close to, the experimental values, which demonstrates the applicability of the VRH approximation scheme to NMC materials. Especially for NMC333, our calculated results for the shear modulus, Young's modulus, and Poisson's ratio (77.95 GPa, 195.06 GPa, and 0.252, respectively) are all surprisingly close to the reported experimental results [37] [(78 ± 1) GPa, (194 ± 2) GPa and 0.25, respectively; this demonstrates the reliability and accuracy of our calculations.

Figure 2 displays the variation trend of the isotropic mechanical properties with the increment of Ni content in various layered NMC materials. As the Ni content increases, the isotropic elastic moduli (including bulk moduli, shear moduli, and Young's moduli) of NMC materials all show an overall trend of decline [Figs. 2(a)–2(c)], although there are still several exceptions. More specifically, the trends of Young's moduli and shear moduli are almost exactly the same, and the opposite trends occur between the pair of NMC442 and NMC552, as well as between the pair of NMC71515 and NMC811. However, the opposite trend occurs only between the pair of NMC442 and NMC552 in the case of bulk moduli.
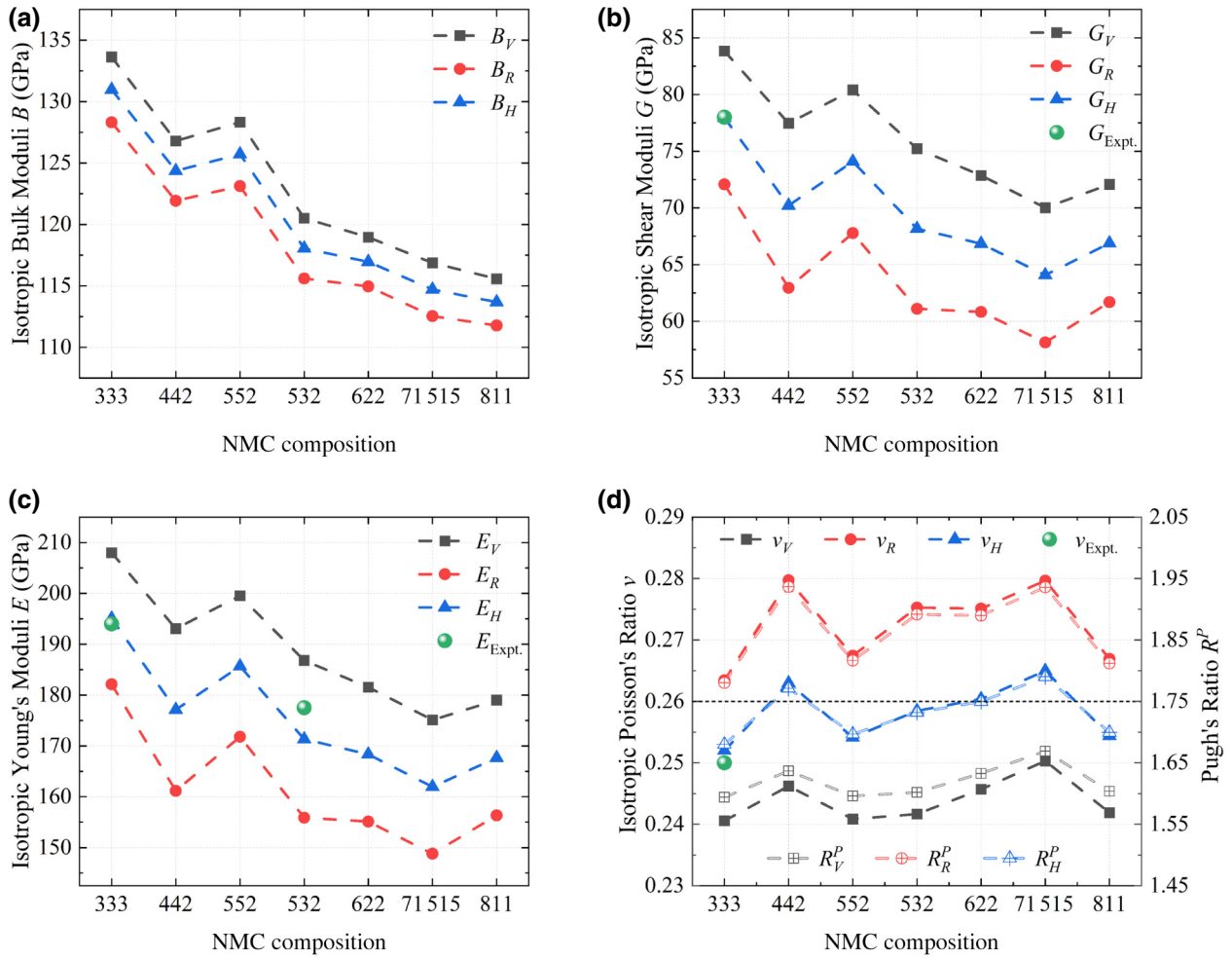
FIG. 2. Average mechanical properties of bulk NMC polycrystal. (a) Isotropic bulk moduli B, (b) isotropic shear moduli G, (c) isotropic Young's moduli E, and (d) isotropic Poisson's ratio ν and Pugh's ratio R^P. Subscripts V, R, and H denote the Voigt, Reuss, and Hill approximations, respectively.

Overall, NMC333, with the lowest Ni content, is the one with the largest Young's modulus, shear modulus, and bulk modulus among all seven NMC materials. NMC71515 is the one with the smallest Young's and shear modulus, and NMC811 is the one with the smallest bulk modulus but, actually, the difference in bulk moduli between NMC71515 and NMC811 is very small (about 1.03 GPa). In fact, for Young's moduli, the trend shown in Fig. 2(c) is very similar to the trend of the previously reported computational results [38], although there is still a slight difference. In their results, since NMC552 and NMC71515 were not included, NMC622 was the one with the smallest Young's modulus (smaller than their value of NMC811); in our results, NMC811 is the one with the smallest Young's modulus, if excluding NMC71515, although the difference between NMC811 and NMC622 is very small (about 0.67 GPa). The overall declining trend of elastic moduli with the increment of Ni content shows that the Ni component contributes less to the elastic moduli than Mn

and Co in NMC materials. As for the two exceptions, i.e., the NMC442 and NMC552 pairs and the NMC71515 and NMC811 pairs, a careful analysis of the components of these two sets of NMC materials reveals that this phenomenon is actually related to the relative proportions of Mn and Co. Compared with NMC442, NMC552 has not only a higher Mn content, but also a lower Co content (see Table S1 within the Supplemental Material [63]), and in fact, NMC552 has the highest Mn content among these seven NMC materials. Therefore, the relatively high elastic moduli of NMC552 seem to show that Mn contributes more to enhancing the elastic moduli than Co in NMC materials. This is also reflected in the case of NMC71515, since the relatively low elastic moduli of NMC71515 could be caused by the fact that the actual Mn content (0.13) is lower than the actual Co content (0.167) in our NMC71515 supercell (see Table S1 within the Supplemental Material [63]). In fact, our results of the relatively high elastic moduli of Mn-rich NMC materials are consistent with the

previously reported experimental results [35], which have shown that Mn-rich NMC materials have higher Young's moduli than Ni-rich NMC materials.

The isotropic Poisson's ratios, v, and Pugh's ratios, R^P [Fig. 2(d)], show exactly the same trends owing to the monotonicity expressed by Eqs. (15) and (16). Furthermore, they show the opposite trend to all three kinds of moduli, i.e., an overall upward trend with an increment of Ni content, except for NMC442 and NMC811. It seems that the one with a relatively small value of modulus has a relatively large value of Poisson's and Pugh's ratios, which is obviously shown in Fig. 2 where the concave points at NMC442 and NMC71515 in Figs. 2(b) and 2(c) exactly correspond to the convex points at NMC442 and NMC71515 in Fig. 2(d). In Fig. 2(d), one of the aforementioned so-called critical values, i.e., $R^P = 1.75$ ($v = 0.26$), is marked with a black dotted line, which is also used as the reference base for the alignment of the left and right vertical axes. As for the other one of the so-called critical values, i.e., $R^P = 2$ ($v = 0.286$), it is approximately equal to the maximum value of the ordinate in Fig. 2(d). If we refer to the first so-called critical criterion, i.e., $R^P = 1.75$ ($v = 0.26$), as done in previous reports [78,79, 83,87,88], the Reuss results seem to classify all the NMC materials as brittle-type materials, while on the contrary, the Voigt results seem to classify all the NMC materials as ductile-type materials. The Hill results seem to classify some of the NMC materials (NMC442, NMC622, and NMC71515) as ductile-type materials, while classifying the others as brittle-type materials. However, all the Voigt, Reuss, and Hill results seem to recognize all the NMC materials as brittle-type materials if we refer to the second so-called critical criterion, i.e., $R^P = 2$ ($v = 0.286$), as done in previous reports [85,86]. In fact, it is worth noting that neither $B/G = 1.75$ ($v = 0.26$) nor $B/G = 2$ ($v = 0.286$) have been mentioned in Pugh's original article [84], and such so-called critical criteria are merely an empirical statistical rule, which is probably summarized by later researchers from a large amount of pure metal data (such as data given in Pugh's original article [84]). Thus, here we point out that such a so-called critical criterion for Pugh's ratio (or Poisson's ratio) is not a universal rule, and these so-called critical values [either $B/G = 1.75$ ($G/B = 0.57$) or $B/G = 2$ ($G/B = 0.5$)] may be applicable to a specific type of material, such as pure metals, but it may not be feasible to generalize them for a variety of materials.

Nevertheless, the method of evaluating the relative ductility or brittleness of a certain type of material by comparing the relative size of the B/G value still has a certain generality because it is based on the following facts, as elucidated by Pugh [84]: the shear modulus of a material is proportional to its ability to resist plastic deformation (namely, the larger the shear modulus of a material, the less likely it is to be plastically deformed), while the bulk

modulus of a material is proportional to its ability to resist fracture (namely, the larger the bulk modulus of a material, the less likely it is to be fractured), and therefore, the ratio of the bulk modulus to the shear modulus can reflect the relative ductility and brittleness characteristics of a material. However, it should also be noted that there may be still a premise for the correct use of Pugh's ratio, that is, a comparison of relative ductility or the brittleness of materials should be limited to a certain type of material with a similar structure. Otherwise, the results may be unreliable due to the differences in crystal structures between the different types of materials. For example, the effect of the crystal structure has been reported in some Laves phases [105].

Here, the various NMC materials have the same layered structures and thus, the Pugh's ratio and Poisson's ratio data in Fig. 2(d) actually show that, roughly speaking, the NMC materials become more ductile with an increment of Ni content, except for NMC442 and NMC811; additionally, NMC442 and NMC71515 show a relatively more ductile characteristic compared with the other NMC materials. This phenomenon may be caused by the variation of moduli, since a material with a smaller modulus is easier to deform elastically under stress, and thus, may be more likely to deform plastically too. Or to put it another way, the Young's modulus (the slope of the linear elastic region of the tensile stress-strain curve) is related to the yield strength (the highest stress point of the tensile stress-strain curve within the range of elastic deformation), which is the most important one among the differently defined strengths of a material, and a material with a higher Young's modulus (i.e., larger slope) usually has a higher yield strength (i.e., larger value of the ordinate of stress) when compared with its counterparts of the same type with similar structures. Furthermore, a material with a higher strength usually shows a tendency to be more brittle. Therefore, the variation trend of Pugh's ratio and Poisson's ratio of NMC materials with an increment of Ni content could be due to the opposite variation trend of elastic moduli.

D. Anisotropic mechanical properties of single crystals of NMC materials

With the increasing application of SNMCs, the primary particle size of NMC materials has increased from the nanometer scale in traditional PNMCs to the micrometer scale in SNMCs. Therefore, understanding the mechanical anisotropy inside the large primary single-crystalline particle becomes more important to address the intragranular cracking issue. The directional Young's modulus given by Eq. (18) indicates that the anisotropic Young's modulus of a single crystal has a spatial dependence and its 3D spatial distribution can be visualized. Likewise, the directional compressive modulus (or linear compressibility), directional shear modulus, and directional Poisson's

ratio can be also visualized. However, the visualization of directional shear modulus and directional Poisson's ratio is a little complicated since the shear modulus and Poisson's ratio depend on two perpendicular directions. When the first vector, **a**, is oriented along a certain direction in 3D space, the second vector, **b**, can rotate at any angle within the plane perpendicular to vector **a**, and thus, the values of shear modulus and Poisson's ratio for each direction can take many different values. Therefore, the two representations of maximum and minimum values were selected to be separately visualized. These 3D visualization results obtained from the VASPKIT [137] tool, and the two-dimensional (2D) projection results obtained from the ELATE [138] tool, of all the studied NMC materials (together with the results of LNO as a reference for the correspondence of orientation) are shown in Figs. S3–S16 within the Supplemental Material [63], from which it can be seen that all the NMC materials have a similar spatial distribution of these anisotropic mechanical

properties, since the orientation of the Cartesian coordinate axes of each NMC material have been adjusted to coincide with that of the hexagonal conventional crystal unit cell (CCUC) of $R\bar{3}m$ LNO in the same manner as that shown in Fig. S17 within the Supplemental Material [63] (also see Sec. S3 within the Supplemental Material [63]). Therefore, here NMC532 is selected as a representative, with its 3D visualization results given in Fig. 3, to study the characteristics of the spatial distribution of these anisotropic mechanical properties. For the sake of convenience, a spherical coordinate system, (r, θ, ϕ), is used for analysis in the following discussion, and its correspondences to the Cartesian coordinate system, $O(x, y, z)$, and the LNO hexagonal CCUC (a, b, c) are shown in Fig. S17 within the Supplemental Material [63].

Figure 3 shows that, except for the Young's modulus [Fig. 3(a)], all the other anisotropic mechanical properties [Figs. 3(b)–3(f)] seem to exhibit local minima along the z-axis direction, while the value of the Young's
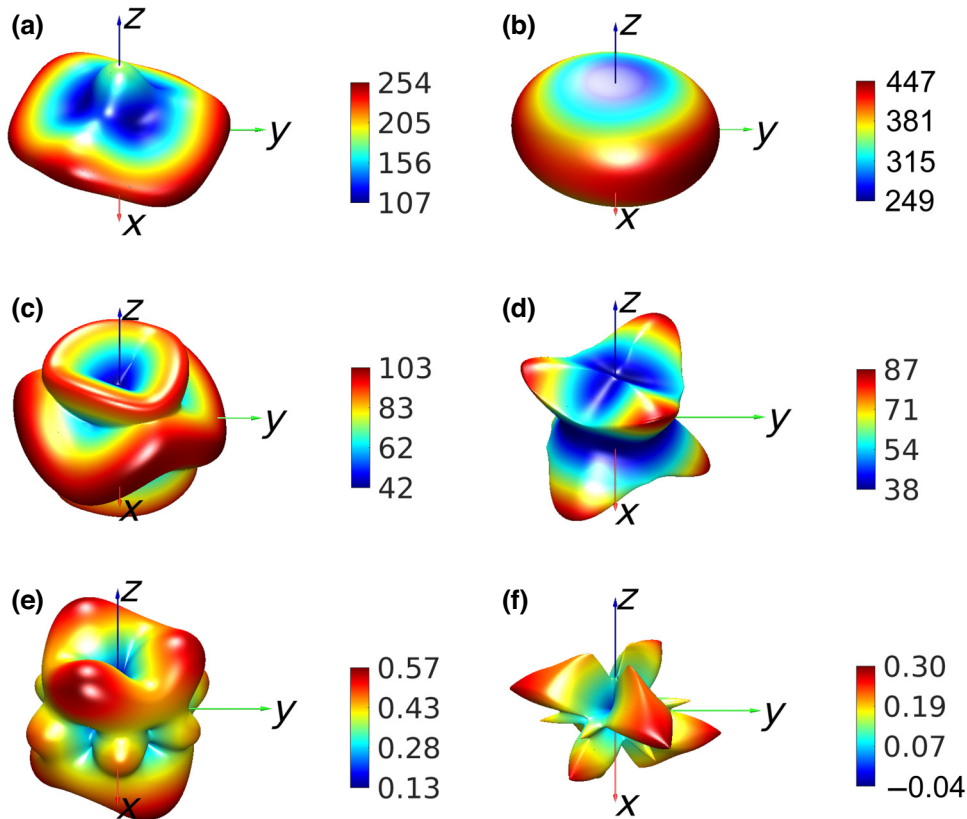

FIG. 3. 3D spatial distribution of the anisotropic mechanical properties of bulk NMC532 single crystal. (a) Directional Young's modulus, (b) directional compressive modulus, (c) directional shear modulus in maximum values, (d) directional shear modulus in minimum values, (e) directional Poisson's ratio in maximum values, and (f) directional Poisson's ratio in minimum values. Distribution directions of maxima and minima can be, respectively, referred to as red and blue areas. Notably, the y-z plane here corresponds to $\phi = 90°$, and thus, corresponds to the $(2\bar{1}0)$ crystal plane, and the six planes obtained by rotating the y-z plane around the z axis at the angles of $\phi = k \times 60°$ ($k = 0, 1, 2, 3, 4, 5$) constitute the crystal planes of the $\{2\bar{1}0\}$ family. Visualization is completed by MATLAB with data processed by the VASPKIT [137] tool. Data of directional compressive moduli were postprocessed by us based on data of directional linear compressibility obtained from VASPKIT. The values of the moduli shown here are in GPa.

modulus [Fig. 3(a)] along the z-axis direction is not a local minimum but is smaller than the values in all directions in the x-y plane. This is actually a reflection of the characteristics of layered materials, in which interlayer interactions are weaker than intralayer interactions. This characteristic is most simply reflected in the compressive modulus [Fig. 3(b)]. Since the compressive modulus refers to the anisotropic modulus of a material under isotropic hydrostatic pressure, strong intralayer interactions lead to maxima of the compressive modulus in all directions in the x-y plane, while weak interlayer interactions lead to a minimum of the compressive modulus along the z axis. Unlike the compressive modulus (and linear compressibility), other mechanical properties are not defined under the condition of isotropic hydrostatic pressure, and thus, exhibit stronger anisotropy. In addition, it is precisely because of this difference that the compressive modulus is much larger than the Young's (tensile) modulus, as the former is restricted in all three directions and the axial compressive deformation cannot be increased through lateral free expansion, while the latter is free in the two lateral directions and the axial tensile deformation can be enhanced by the accompanying lateral free contraction (which is the origin of Poisson's ratio). Next, we specifically discuss the orientations of the maxima and minima of these significantly anisotropic mechanical properties. These extreme values are the most direct reflection of the anisotropy and play a crucial role in understanding the anisotropic elastic mechanical characteristics of NMC materials.

Except for the compressive modulus [Fig. 3(b)], the spatial distributions of the Young's modulus [Fig. 3(a)], shear modulus [both Figs. 3(c) and 3(d)], and Poisson's ratio [both Figs. 3(e) and 3(f)] all exhibit an approximate trigonal symmetry, to some extent. Each of them has (at least) six global maxima (red areas in Fig. 3), and the directions in which the six global maxima appear are all distributed at intervals of 60° around the z axis. Moreover, three of them, distributed at intervals of 120°, constitute an upward layer ($\theta < 90°$), and the other three constitute a downward layer ($\theta > 90°$). More specifically, in the spherical coordinate system (r, θ, ϕ), the directions of their respective six global maxima all satisfy $\phi = 30° + k \times 60°$ ($k = 0, 1, 2, 3, 4, 5$) and $\theta < 90° \ \forall \ k = 1, 3, 5$ ($\theta > 90° \ \forall \ k = 0, 2, 4$) for Figs. 3(a) and 3(e), while, on the contrary, $\theta > 90° \ \forall \ k = 1, 3, 5$ ($\theta < 90° \ \forall \ k = 0, 2, 4$) for Figs. 3(c), 3(d), and 3(f). In fact, as shown in Table S6 within the Supplemental Material [63], the specific directions of these maxima lie within the six crystallographic planes of the $\{2\bar{1}0\}$ family of planes. Notably, the $(2\bar{1}0)$ crystal plane corresponds to $\phi = 90°$, and thus, corresponds to the y-z plane in Fig. 3, and the other five crystal planes in the $\{2\bar{1}0\}$ family refer to the planes obtained by rotating the y-z plane around the z axis at angles of $\phi = k \times 60°$ ($k = 1, 2, 3, 4, 5$). For LNO with

the highest symmetry, the specific directions of these maxima are listed in Table S7 within the Supplemental Material [63], which can serve as a reference for NMC materials, since they exhibit similar results (as observed from Figs. S3–S8 within the Supplemental Material [63]). However, due to certain deviations in the lattice symmetry of NMC materials, these six maxima are not exactly equal but only approximately equal, and there may be some discrepancies in the orientations of these maxima compared to data in Table S7 within the Supplemental Material [63]. The distortions caused by these deviations can be well observed from the 2D projections shown in Figs. S9–S16 within the Supplemental Material [63].

Regarding the minima, an interesting point is that there are also six global minima of Young's modulus [blue areas in Fig. 3(a)], and they always appear in pairs with maxima at the same angle ϕ (but at different angle θ, see Table S7 within the Supplemental Material [63]). For the shear modulus, the situation is a bit special, with 12 global maxima in Fig. 3(c) and 12 global minima in Fig. 3(d), the specific orientations of which can be referenced to that of LNO given in Tables S7 and S8 within the Supplemental Material [63]. When first vector **a** is along the z-axis direction (i.e., $\theta = 0°$), no matter which direction second vector **b** takes, the shear modulus always takes the same local minimum [i.e., the values of shear modulus along the z axis in both Figs. 3(c) and 3(d) are equal]. However, when first vector **a** lies in the x-y plane and points along any of the six crystallographic directions of the $\langle 100 \rangle$ family of directions, the shear modulus can take either a global maximum [red areas in Fig. 3(c)] or global minimum [blue areas in Fig. 3(d)], depending on the specific orientation of second vector **b**. The other six global maxima and minima of the shear modulus all appear within the six crystal planes of the $\{2\bar{1}0\}$ family. As for the situation of Poisson's ratio, there are also twelve maxima in Fig. 3(e) and twelve minima in Fig. 3(f), and their specific orientations are also similar with those of the shear modulus (i.e., with the same ϕ for all, but different θ for some). However, among these 12 maxima and 12 minima, there are only six global maxima and six global minima, with the former located within the six crystal planes of the $\{2\bar{1}0\}$ family [red areas in Fig. 3(e)] and the latter along the six crystal directions of the $\langle 100 \rangle$ family within the x-y plane [blue areas in Fig. 3(f)]. The other six maxima and minima are local rather than global. Additionally, it is special that there are two sets of six local maxima of Poisson's ratio in Fig. 3(f) (small yellow fangs), both of which pair with each other at the same angle ϕ (but at different angle θ) and are all located within the six crystal planes of the $\{2\bar{1}0\}$ family.

Interestingly, Figs. 3(e) and 3(f) (as well as Figs. S7 and S8 within the Supplemental Material [63]) show that the global maxima of Poisson's ratio have exceeded the theoretical range $(-1, 0.5)$ for the isotropic Poisson's ratio, and the global minima of Poisson's ratio for many NMC

materials are negative. Actually, the theoretical range $(-1, 0.5)$ is for the isotropic Poisson's ratio, and the anisotropic Poisson's ratio is not subject to this restriction [139], so it is possible to exceed this range. In contrast to the maxima, the negative minima of Poisson's ratio deserve more attention, as the negative Poisson's ratio of a material is a rare phenomenon and is usually accompanied by some novel properties. Materials with negative Poisson's ratio are known as auxetics [139] and have been more and more extensively studied [89,139–143] since the first report by Lakes [144]. In addition, it is worth mentioning that spinel $LiNi_{0.5}Mn_{1.5}O_4$, another cathode material for LIBs, has been reported [145] to exhibit auxeticity after delithiation at high voltage. Nevertheless, here some NMC materials are found to exhibit auxeticity in several directions before delithiation, although the values of these negative Poisson's ratios are so close to zero that they can even be considered to result from the fluctuation within the error range of numerical calculations. In fact, in contrast to the rare isotropic auxetic, the directional auxetic properties of anisotropic materials are quite common, as it was reported [140,142] that 69% of the cubic elemental metals exhibited auxetic behavior in at least one direction; these materials are known as partial auxetics [142]. Therefore, it is perhaps not surprising that NMC materials may exhibit partial auxetic properties. However, considering that the Poisson's ratio of NMC materials is positive in most directions in 3D space, it is currently unclear whether the negative minima of Poisson's ratio, which appear in only a few directions, can bring about other special properties for NMC materials. Perhaps further study can reveal the potential application of the peculiar phenomenon of the anisotropic Poisson's ratio of NMC materials.

On the whole, from Fig. 3, it can be observed that the global maxima and minima of various anisotropic mechanical properties all appear in certain directions within the six crystal planes of the $\{2\bar{1}0\}$ family (also see Table S7 within the Supplemental Material [63]), except for the global minima of Poisson's ratio, which appear along the six crystal directions of the $\langle 100 \rangle$ family (also see Tables S8 and S9 within the Supplemental Material [63]). Additionally, the other six global maxima and minima of the shear modulus also repeatedly appear in directions of the $\langle 100 \rangle$ family (also see Tables S8 and S9 within the Supplemental Material [63]). It should be noted that, in layered NMC materials, the $\langle 100 \rangle$ crystal direction family actually are the intralayer close-packing directions and are the intersection lines between the intralayer (001) close-packing plane and the interlayer sparse-packing planes of the $\{010\}$ family. On the other hand, the members of the $\{2\bar{1}0\}$ crystal plane family are actually the interlayer close-packing planes, and their intersection lines with the intralayer (001) close-packing plane correspond to the $\langle 120 \rangle$ crystal direction family, which are the intralayer sparse-packing directions. Their relationships can be seen in Tables S5

and S6 within the Supplemental Material [63], as well as in Fig. S18 within the Supplemental Material [63], which displays the lattice packing directions of the $(2\bar{1}0)$, (010), and (001) planes. In fact, these three planes correspond to the y-z, x-z, and x-y planes, respectively, and thus, correspond to the projection planes of the 2D projection plots of various mechanical properties shown in Figs. S9–S16 within the Supplemental Material [63]. Thus, the difference in mechanical anisotropy among these three planes can be roughly observed from the projection plots. On the other hand, our custom-defined average anisotropy parameter (see Table S10 within the Supplemental Material [63]) indicates that, taking into account various mechanical properties, the order of mechanical anisotropy strength for these three planes is y-z plane $> x$-z plane $> x$-y plane $(1.73 > 1.59 > 1.27)$. In other words, the $\{2\bar{1}0\}$ crystal plane family contains the most significantly anisotropic planes for NMC materials; this is obviously related to the special lattice packing pattern within the $\{2\bar{1}0\}$ crystal plane family. Therefore, the direction of lattice packing within the $(2\bar{1}0)$ crystal plane and the directions of the global maximum and minimum of the Young's modulus of the simplest LNO are shown in Fig. S19 within the Supplemental Material [63] as an example to demonstrate such relations. It can be noted that the close-packing direction within the $(2\bar{1}0)$ crystal planes consists of parallel Li-TM-Li atomic chains and is actually the $[\bar{4}\bar{8}1]$ crystal direction (see Fig. S19 within the Supplemental Material [63]). The direction of the global maximum of the Young's modulus spans the parallel Li-TM-Li atomic chains at a certain angle (about 47°, see Fig. S19 within the Supplemental Material [63]), while the direction of the global minimum of the Young's modulus is along the gap between the two parallel Li-TM-Li atomic chains (with a very small angle of about 5° to the Li-TM-Li atomic chain). Considering the fact that the $[\bar{4}\bar{8}1]$ close-packing direction within the $(2\bar{1}0)$ crystal planes is actually the intersection line between the $(2\bar{1}0)$ and (104) planes (as can be seen in Fig. S20 within the Supplemental Material [63]); therefore, the direction of the global minimum of Young's modulus is also between two parallel (104) planes. This means that the (104) plane and $[\bar{4}\bar{8}1]$ direction are prone to be the cleavage plane and cleavage direction, respectively, along which microcracks and even mechanical failures may be susceptible to occur due to stress concentration. A more detailed discussion is given below Fig. S19 within the Supplemental Material [63].

Similar to the isotropic mechanical properties, we are also concerned about whether the anisotropic mechanical properties of various NMC materials are related to the composition differences in NMC materials. Although the anisotropic mechanical properties of various NMC materials have similar spatial distributions (see Figs. S3–S8 within the Supplemental Material [63]), there are differences in the magnitudes between their respective maxima
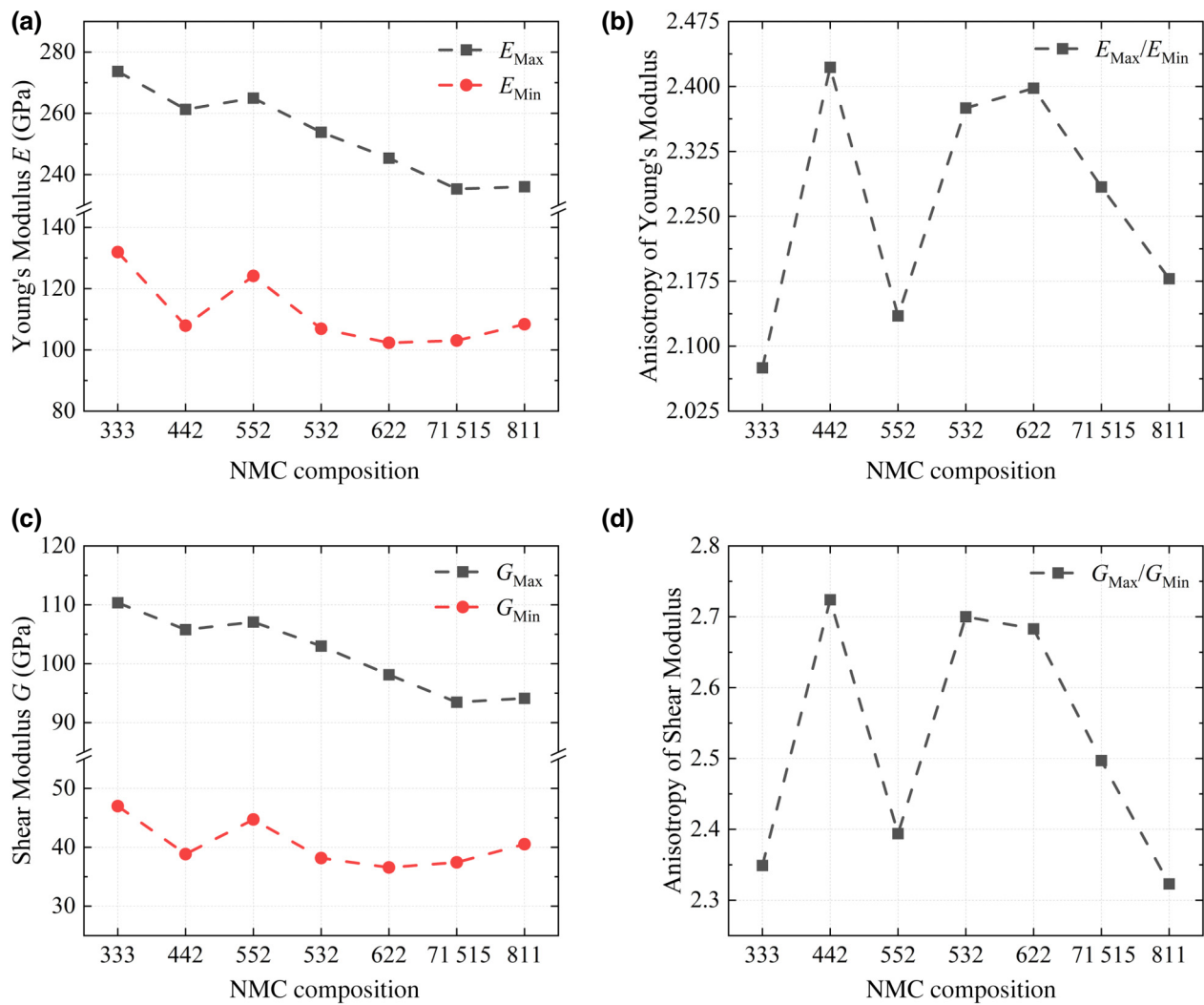
FIG. 4.   Maximum and minimum values of anisotropic (a) Young's modulus and (c) shear modulus of bulk NMC single crystal. (b),(d) Assessment of their corresponding anisotropies by the custom-defined anisotropy parameters.

or minima. Therefore, the maxima and minima of the anisotropic mechanical properties are taken out and then their variation trends with the increment of Ni content in various layered NMC materials are drawn in Figs. 4 and S21 within the Supplemental Material [63], in which the corresponding custom-defined anisotropy parameters are also shown. Figure 4 shows that the maxima and minima of the anisotropic Young's and shear moduli display a similar overall decline trend and the same convex point at NMC552 and concave point at NMC71515 with the isotropic Young's and shear moduli shown in Fig. 2. In addition, the custom-defined anisotropy parameters of Young's and shear moduli [Figs. 4(b) and 4(d)] all indicate that the elastic anisotropies of NMC333, NMC552, and NMC811 are lower than the others. In particular, NMC442 shows the highest elastic anisotropy. Therefore, from the perspective of the anisotropic Young's and shear moduli, NMC442 shows relatively poor mechanical

performance, not only with relatively small maximum and minimum values but also with relatively high anisotropy. On the contrary, NMC552 has a better mechanical performance, with relatively larger maximum and minimum values and relatively lower anisotropy. Similarly, the contrast between NMC71515 and NMC811 shows a similar comparative relationship between NMC442 and NMC552. These results indicate that the role of Mn is beneficial not only for enhancing the elastic moduli (similarly to the case of the above isotropic mechanical properties), but also for reducing the mechanical anisotropy of NMC materials. On the whole, among the seven NMC materials studied here, NMC333 shows the best mechanical performance in terms of anisotropic Young's and shear moduli, not only with the largest maximum and minimum values but also with almost the lowest elastic anisotropy. Regarding the compressive modulus, the variation trends of its maxima and minima are also similar to those of the

isotropic elastic moduli, but the anisotropy parameter indicates that NMC811 has the highest anisotropy in terms of compressive modulus (see Fig. S21 within the Supplemental Material [63]), which is different from the case of the anisotropic Young's and shear moduli. As for the anisotropic Poisson's ratio, the variation trend of its maxima is consistent with the isotropic Poisson's ratio, while that of its minima is different and even shows almost the opposite trend to its maxima (see Fig. S21 within the Supplemental Material [63]). This may be ascribed to the negative minima of the anisotropic Poisson's ratio of some NMC materials. Lastly, the variation trend of the anisotropy parameters of the anisotropic Poisson's ratio is also similar to that of the anisotropic Young's and shear moduli.

Evaluating the elastic anisotropy of various NMC materials is of significant importance, as the smaller the elastic anisotropy, the lower the likelihood of stress concentration and subsequent failure within the material. The custom-defined anisotropy parameters generally reflect the anisotropy of each kind of mechanical property of NMC materials quite well. However, the results they give are not entirely consistent. Although this can be understood as the same NMC material having different anisotropy characteristics of different mechanical properties, on the contrary, it also indicates a lack of generality in these custom-defined anisotropy parameters of the four mechanical properties. Therefore, to comprehensively consider the anisotropy of various mechanical properties, a universal measure of mechanical anisotropy is required. The aforementioned universal elastic anisotropy index, A^U, and Kube's log-Euclidean elastic anisotropy index, A^L, can precisely fulfill this role, as they consider both the bulk and shear contributions from the perspective of the Voigt and Reuss estimations of elastic constants, as seen from their expressions given in Eqs. (24) and (25). A^U and A^L are calculated for various NMC materials and their Ni content dependent variation trends are plotted in Fig. 5, from which it can be observed that the variation trends of A^U and A^L are synchronized. Figure 5 bears some resemblance to Figs. 4(b) and 4(d), as they all indicate that NMC333, NMC552, and NMC811 have a relatively low elastic anisotropy compared to other NMC materials. However, there are also significant differences, particularly for the NMC622 material. In Figs. 4(b) and 4(d), the anisotropy of the Young's and shear moduli of NMC622 is significantly higher than that of NMC71515, while A^U and A^L in Fig. 5 show that the elastic anisotropy of NMC622 is slightly lower than that of NMC71515. This is because, as aforementioned, A^U and A^L take into account both the bulk and shear contributions; besides, the anisotropy of the compressive modulus, which has a certain correlation with the bulk modulus, of NMC622 is quite low [see Fig. S21(b) within the Supplemental Material [63]]. In addition, another special case is NMC811, which has the highest anisotropy of the compressive modulus [see Fig. S21(b) within the Supplemental Material [63]], yet still has relatively small values of A^U and A^L, owing to its relatively low anisotropy of the shear modulus. Therefore, A^U and A^L can more comprehensively reflect the mechanical anisotropy of NMC single crystals because they consider the contributions from different mechanical properties. Finally, since A^L is devised to be capable of comparing the multiplicative relationship between two crystals, it can be concluded that, among these seven studied NMC materials, the NMC532 crystal has the strongest elastic anisotropy, while the NMC333 crystal has the weakest elastic anisotropy, and the elastic anisotropy of the former ($A^L = 0.466$) is 1.37 times greater than that of the latter ($A^L = 0.34$).
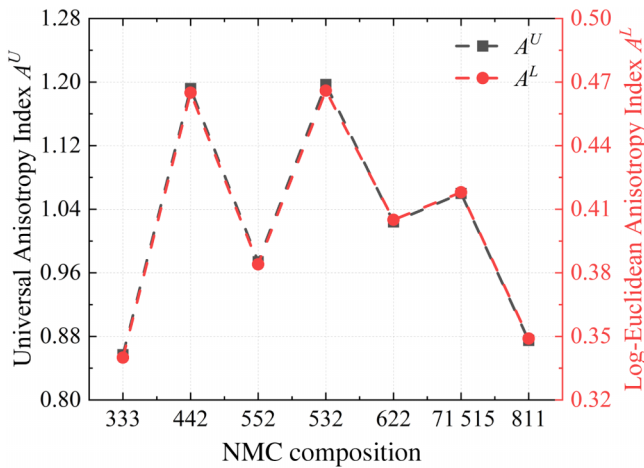

FIG. 5. Universal elastic anisotropy index, A^U, and Kube's log-Euclidean elastic anisotropy index, A^L, of bulk NMC single crystals.

E. Cauchy pressures and bonding characters

The Cauchy pressures are calculated with Eq. (30) rather than Eq. (31) because the relations of $C_{44} = C_{55}$ and $C_{13} = C_{23}$ are not satisfied for our calculated elastic constants of NMC materials due to their reduced symmetry. The results of all the NMC materials calculated based on our computational elastic constants are listed in Table S11 within the Supplemental Material [63], and it is shown that the values of P_{xy}^{Cauchy} are all negative for all the NMC materials, while the values of P_{yz}^{Cauchy} and P_{zx}^{Cauchy} are almost all positive (except for NMC333 and NMC811, with negative but quite small values). Before discussing the implications of these results, the physical meaning of the Cauchy pressure should be carefully checked, since the description of the bonding characters predicted by the Cauchy pressure is still incomplete and even inappropriate in a large amount of the literature. Usually, most reports simply

classify the positive Cauchy pressure (PCP) as a metallic bonding character and the negative Cauchy pressure (NCP) as a covalent bonding character, while ionic bonding is missing because the ionic bonding effect is negligible in the alloy systems discussed in these reports. However, when the Cauchy pressure was extended to ionic crystals in several papers [83,97,126,146–149], the NCP was also described as a covalent bonding character, but the PCP was described as an ionic bonding character and metallic bonding was not discussed. A comprehensive discussion of the relations of all the three types of bonds and the Cauchy pressure is rarely reported. Therefore, here we point out that, taken together, the NCP reflects the covalent bonding character, but the PCP should be able to reflect either metallic or ionic bonding characters, depending on the systems studied. Based on a mechanism-oriented analysis, the reason can be elucidated as follows. According to Eq. (30), an NCP means that the shear components (C_{44}, C_{55}, and C_{66}) are larger than the corresponding volume components (C_{23}, C_{13}, and C_{12}, see the discussion below), which means that the ability to resist shear deformation (which is bond bending dominated) is stronger than the ability to resist volumetric deformation (which is bond stretching dominated). Thus, as previously reported, the NCP reflects the angular dependent many-body interactions [100,109,115,150], which result in a directional bonding character [106,151] with strong resistance to interatomic bond bending [106,150,151], and actually, all these characters are the nature of the covalent bonding interaction. On the contrary, both metallic and ionic bonding are governed by the electrostatic interaction, which is a kind of central force (i.e., forces related only to the distance but not direction characterized by angles), and thus, is not resistant to bond bending. Therefore, for metallic and ionic bonding, bond stretching is dominant during deformation, which means that the volume components (C_{23}, C_{13}, and C_{12}, see the discussion below) are larger than the corresponding shear components (C_{44}, C_{55}, and C_{66}), and this results in a PCP. This analysis of the Cauchy pressure is consistent with previous reports on the bonding characters predicted by the isotropic Poisson's ratio. On the one hand, it was reported [125,127,128,152] that for typical covalent, ionic, and metallic materials, the values of the isotropic Poisson's ratio were about 0.1, 0.25, and 0.33, respectively. On the other hand, it was also reported [125,127,153] that, for central forces in crystals, the lower and upper limits of the isotropic Poisson's ratio were 0.25 and 0.5, respectively. In addition, these reports on the relations of Poisson's ratio and bonding characters demonstrated that the Cauchy pressure might have some connection to Poisson's ratio, and thus, Pugh's ratio.

In fact, the Cauchy pressure is indeed related to Pugh's ratio and Poisson's ratio, and we find that the relations between these three parameters can be seen as follows. Notably, in Eq. (30), C_{44}, C_{55}, and C_{66} are all the shear components of elastic constants; C_{12}, C_{13}, and C_{23} are all the components related to lateral deformation, which is related to Poisson's ratio, as shown in Eq. (20), and thus, related to volume changes [78,79]. Therefore, it can be found that the Cauchy pressure is similar to Pugh's ratio, since both are comparing shear deformations to volume changes. The difference between the two lies in the starting point of consideration. The former is considered from the anisotropic elastic constants of single crystals, while the latter is considered from the isotropic elastic moduli of polycrystals. Actually, similar to Pugh's ratio and Poisson's ratio, the Cauchy pressure has also been used to evaluate the relative ductility of materials by assuming that the NCP corresponds to brittle character, while the PCP corresponds to ductile character. This is because the characteristic of resistance to bond bending of a covalent bond with an NCP reflects the resistance to shear behavior, and thus, reflects the resistance to plastic deformation. However, here we emphasize that such use of the Cauchy pressure for evaluating the relative ductility of materials is only applicable to systems concerned with covalent bonding because for metallic and ionic bonding systems, although the former is generally more ductile than the latter, this comparison relationship cannot be well manifested by the PCP. Furthermore, whether it is a metal (alloy) or an ionic compound crystal system, the Cauchy pressure can actually be either positive or negative, depending on the contribution of covalent bonding in the crystal. For instance, it was reported [112,127,154] that ionic crystals could have both a large PCP (RbF) or a large NCP (MgO). Besides, although most metals have a PCP, there are still some metals that have a small NCP, such as iridium [155–157], rhodium [156–158], and many transition-metal-based intermetallic compounds [156,157]. However, the ductility of ionic crystals (such as RbF) with a large PCP may not be as good as that of metallic crystals (such as iridium) with a small NCP. Therefore, the use of the Cauchy pressure for ductility evaluation is not convenient and sometimes may not be correct, and hence, we suggest that the Cauchy pressure might only be used for bonding character analysis at best.

Here, in our calculated Cauchy pressure results for NMC materials, all the negative values of P_{xy}^{Cauchy} imply that the intralayer directional bonds have a significant covalency, while nearly all the positive values of P_{yz}^{Cauchy} and P_{zx}^{Cauchy} imply that the interlayer directional bonds are nearly ionic bonding dominated. To better understand these results, one should review the crystal structure features of layered NMC materials. In layered NMC materials, the O ions constitute the O3 close-packing framework (i.e., in a sequence of …ABCABCA… along the *c*-axis direction) of the crystal structure, with the TM and Li ions alternately filling the O close-packed octahedral interstitial layers, as shown in Fig. 1(c). Hence, in the intralayer direction, every two O ions are connected by two TM–O bonds

in the manner of O−TM−O and by two Li−O bonds in the manner of O−Li−O, while in the interlayer direction between two TMO_6 slabs, every two O ions are connected by four Li−O bonds in the manner of two O−Li−O bonding chains. Therefore, the Cauchy pressure results actually imply that the Li−O bonds are nearly ionic bonding dominated, while the TM−O bonds have significant covalency. This is consistent with our intuition and is further proved through the quantitative chemical bond analysis given in the following sections.

In addition, we also calculated the Cauchy pressures of NMC622 based on the recently reported [44] elastic constants from experimental measurements, and the results (also listed in Table S11 within the Supplemental Material [63]) show that the three Cauchy pressures all have very large values, and more importantly, the signs of them are not correct. This demonstrates that the elastic constants from their experimental measurements are not precise. In fact, as pointed out by themselves, their results had quite a large range of deviations, especially for C_{11} and C_{12}. Actually, the deviation of C_{44} in their results is also quite large (which they did not discuss but can be observed from the error bar in their figure). Thus, the large deviations of their C_{11}, C_{12}, C_{44}, and also C_{66} (noting that $C_{66} = (C_{11} - C_{12})/2$ in their assumption, which approximately recognizes that NMC622 belongs to the trigonal crystal system) lead to the wrong results for the Cauchy pressures. Additionally, it may be noted that the Cauchy pressure of layered $LiNi_xCo_{1-x}O_2$ cathode materials has also been reported in a recent study [99], but unfortunately, their results with large positive values are not correct because they have misused the relationship of $C_{12} - C_{44}$, which is only applicable to the cubic crystal system and not to their trigonal crystal system.

F. Chemical bond analysis for a deeper understanding of mechanical properties

The above analysis of the roles of the Ni, Mn, and Co components on the mechanical properties of NMC materials reveals that the contributions of components to enhancing the elastic moduli in NMC materials are in the order of Mn > Co > Ni, which is inferred from the results and the reasons behind them have not been explored yet. Actually, in terms of the reason for the declining trend of Young's moduli with increasing Ni content in NMC materials, Sun and Zhao [38] proposed a rough qualitative explanation that focused on the variation of valence electron density resulting from the variation of average ionic size. They only considered the influence of Ni content and the variation of the ionic size of Ni ions, but ignored the difference in the number of valence electrons of various NMC materials and the effect of different Co stoichiometries. However, the factors ignored by them may actually be important. For example, the variation of the

ionic size of Co ions is also an important factor, as seen from the variation of TM−O bond length shown in Fig. S22 within the Supplemental Material [63]. Besides, the above bonding characters predicted by the Cauchy pressures are just qualitative results. Therefore, here we introduce a quantitative description method based on chemical bond analysis to explain the variation trend of elastic moduli with the variation of stoichiometric ratios of TM atoms in NMC materials, and to explain the qualitative Cauchy pressure results.

From a macroscopic point of view, the elastic modulus of a material characterizes the ability to resist elastic deformation under stress, i.e., the larger the elastic modulus, the harder it is to deform a material. In contrast, from a microscopic perspective, the elastic modulus represents the strength of interactions between atoms, i.e., the interatomic binding force or binding energy, and thus, the larger the elastic modulus, the greater the interatomic binding force. The interatomic interactions can be described either by the interaction potential (or force) function curve or by the strength of a chemical bond. The chemical bond in a solid crystal can be described by the concept of the crystal orbital Hamilton population (COHP) [159], which partitions the band-structure energy of a crystal into the bonding, nonbonding, and antibonding contributions. The projected COHP (PCOHP) [160,161] can extract chemical bonding information from our plane-wave-based DFT results, and its integral (i.e., IPCOHP), from the lowest occupied bands up to the highest occupied bands (i.e., the Fermi level) for each chemical bond accounts for its contribution to the band-structure energy of a crystal, and hence, gives the bond strength measurements [160]. In addition, the TM−O bonds in NMC materials commonly consist of a mixture of ionic and covalent bonding, and their contributions to the bond strength have all been described by the IPCOHP values, while the contributions of covalent bonding to the TM−O bonds can be separately quantified by the crystal orbital bond index (COBI) [162] as its integral (i.e., ICOBI) equals the chemical bond order. Therefore, the PCOHP and COBI calculations were carried out in the LOBSTER package [163,164] to obtain information about the chemical bond strength of the studied NMC materials. Since the contribution to the energy of bonding mainly comes from the nearest M−O ($M =$ Li, Ni, Mn, Co) bonding interaction in layered NMC materials, the IPCOHP and ICOBI values were calculated for each M−O bond of various NMC materials. Then, the average IPCOHP and ICOBI values were separately calculated for each species of Li−O, Ni−O, Mn−O, and Co−O bonds, respectively. And finally, their overall averages of all the M−O bonds were calculated. All these results are depicted in Figs. 6 and S23 within the Supplemental Material [63]. Notably, the IPCOHP values are negative because they represent the energy of bonding, and the smaller the IPCOHP values (namely, the greater its
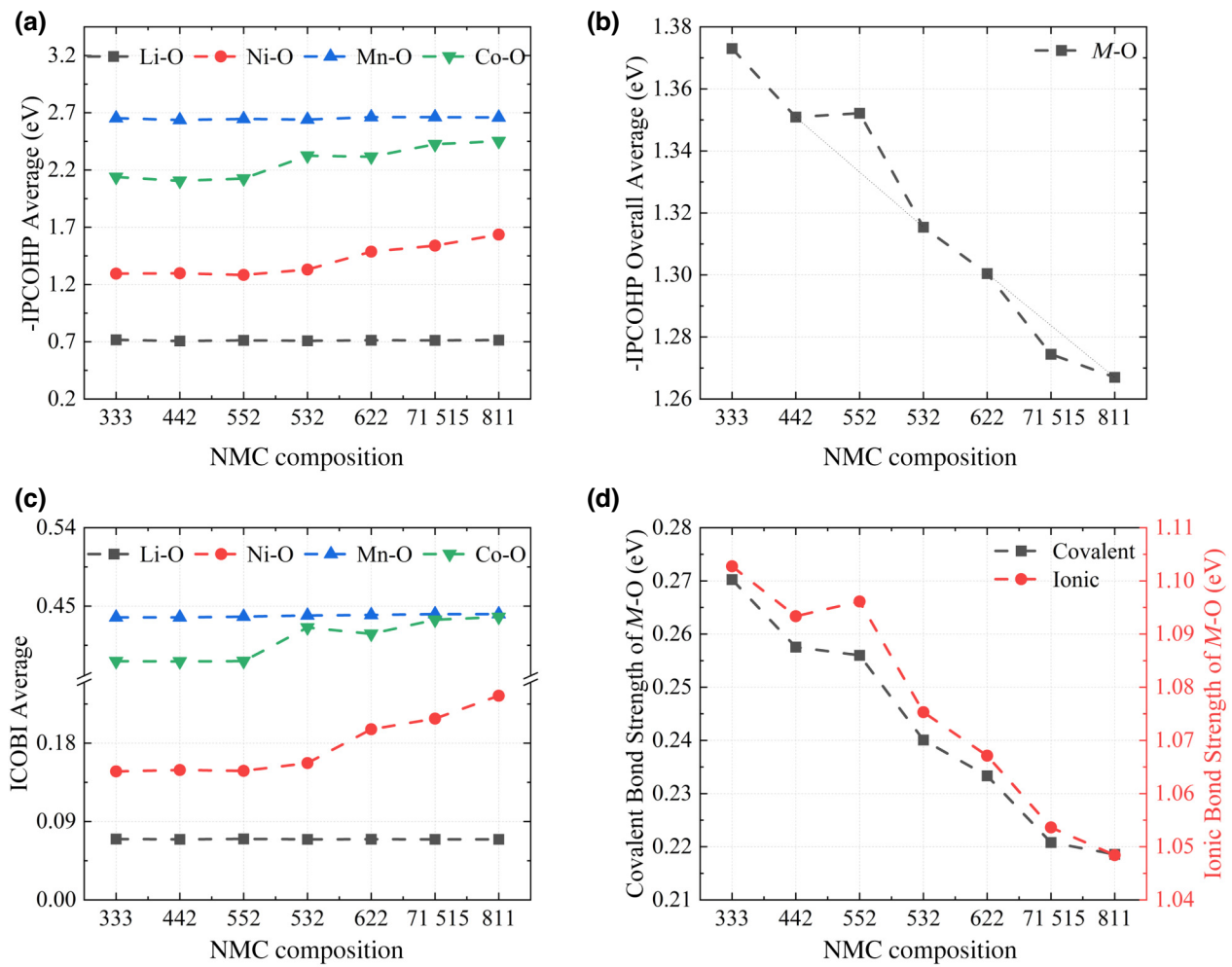
FIG. 6. $M-$O bond strengths in various NMC materials. (a) $-$IPCOHP average of each $M-$O bond species, (b) $-$IPCOHP overall average of all the $M-$O bonds, (c) ICOBI average of each $M-$O bond species, and (d) overall average covalent and ionic bond strengths of all the $M-$O bonds. $M=$ Li, Ni, Mn, Co.

absolute value), the stronger the bond, that is, the negative value of IPCOHP (i.e., $-$IPCOHP) is positively correlated with the bond strength. Therefore, the $-$IPCOHP value, instead of the IPCOHP value, is depicted in Fig. 6 for the convenience of viewing.

The $-$IPCOHP averages for each type of $M-$O bond in Fig. 6(a) clearly show that the bond strength of $M-$O in all NMC materials is in the order of Mn$-$O $>$ Co$-$O $>$ Ni$-$O $>$ Li$-$O, although the bond strength of Ni$-$O and Co$-$O is increased with the increment of Ni content in NMC materials due to the increase of the average valence state. This result provides direct proof for our previous inference that Mn contributes more than Co, and they both contribute more than Ni, to enhancing the elastic moduli of NMC materials. Furthermore, for all the NMC materials, the average $-$IPCOHP values of TM$-$O bonds are all obviously much larger than the average $-$IPCOHP values of Li$-$O bonds. This result corresponds to the above discussion of the characteristics

of the elastic constants of layered materials, as shown in Eqs. (33) and (34).

Figure 6(b) shows that the overall average bond strength of all $M-$O bonds displays an overall declining trend, which is surprisingly consistent with the trends of the elastic moduli shown in Figs. 2 and 4. Moreover, even the convex point at NMC552 and the concave point at NMC71515 in Figs. 2(a)–2(c) and in Figs. 4(a) and 4(c) are consistently shown again in Fig. 6(b). Therefore, the overall average of the $-$IPCOHP of all $M-$O bonds could be a good quantity to describe the variation trend of elastic moduli with the variation of stoichiometric ratios of TM atoms in NMC materials. It is evident that the appearance of the trend in Fig. 6(b) results from not only the difference in average bond strength of each type of $M-$O bond [Fig. 6(a)], but also the difference in the quantities of each type of $M-$O bond, i.e., the specific TM composition proportions [see Fig. S24(a) within the Supplemental Material [63]]. Therefore, combining these two factors,

the summation results of $-$IPCOHP counted in formula units [i.e., one unit of Li(TM)O$_2$] for each M–O species are given in Fig. S24(b) within the Supplemental Material [63]; these explain the trend and the convex and concave points in Fig. 6(b). More details can be found in the discussion below Fig. S24 within the Supplemental Material [63].

The ICOBI value of a chemical bond is in the range of [0,1], and the larger (the closer to one) the ICOBI value, the higher the covalency of a chemical bond; conversely, the smaller (the closer to zero) the ICOBI value, the higher the ionicity of a chemical bond. Therefore, the average ICOBI values shown in Fig. 6(c) clearly demonstrate the mixing nature of TM–O bonds in NMC materials. Figure 6(c) indicates that all types of TM–O bonds in NMC materials have a significant contribution from covalent bonding, especially the Mn−O and Co−O bonds. However, even the highest average ICOBI value of Mn−O (approximately 0.44) is still smaller than 0.5, which implies that all TM–O bonds in NMC materials are still dominated by ionic bonding. Besides, Fig. 6(c) also shows that the Li−O bond, with a very low value of ICOBI (about 0.07), is almost a purely ionic bond, which is commonly accepted knowledge, and hence, proves the reliability of ICOBI analysis. These ICOBI results directly provide the quantitative proof for the above qualitative analysis of the chemical bonding characters by the Cauchy pressures of NMC materials. Therefore, in addition to the weak bond strength of the Li−O bond, as indicated by the $-$IPCOHP value, the low covalency of the Li−O bond, as indicated by both the Cauchy pressure above and the ICOBI value here, demonstrate that the Li−O bonds between the two TMO$_6$ slabs are not resistant to bond bending, and hence, are not resistant to shear deformation. This is the reason why the interlayer glide occurs easily in layered NMC cathode materials, especially in the delithiated states when a lot of Li−O bonds disappear.

The overall average covalent bond strength and ionic bond strength of all the M−O bonds can be separately obtained through the combination of the ICOBI overall average of all the M−O bonds (shown in Fig. S23 within the Supplemental Material [63]) and the $-$IPCOHP overall average of all the M−O bonds [shown in Fig. 6(b)]; the results are depicted in Fig. 6(d). There is an interesting phenomenon in Fig. 6(d) in which NMC552 has a higher ionic bonding strength but a lower covalent bonding strength than NMC442, which implies that the higher bond strength [Fig. 6(b)] and higher elastic modulus [Figs. 2(a)–2(c), 4(a) and 4(c)] of NMC552 than NMC442, caused by the higher Mn content, mainly results from the enhanced contribution of ionic bonding rather than covalent bonding of Mn−O. Considering that Mn ions have the highest average valence state (+4) in NMC materials, the strong ionic bonding of the Mn−O bond is easy to understand. This suggests that doping the other high-valence-state ions in NMC materials

may also have a positive effect on improving their mechanical performance by enhancing the elastic properties. As recently reported often in the literature, the doping of high-valence-state ions (such as Mo^{6+}, Ta^{5+}, Nb^{5+}, and Ti^{4+}) can effectively enhance the cycling performance of NMC [165], Co-free NMC [166–168], and Mn-free NMC [169,170] materials; this has been attributed to factors such as stabilization of surfaces and lattice [165], reduction of volumetric strain [167], refinement of the primary particle size [166], stabilization of the delithiated cathode structure through the Li-TM cation-ordered superlattice [166,170], aligned crystallographic texture of primary particles [169], and modified grain microstructures [170]. However, the improvement effect of high-valence ion doping on the elastic mechanical properties of NMC materials has been overlooked.

Finally, it may be noted that the average bond strength of M−O is more correctly measured by the average $-$IPCOHP values [Fig. 6(a)] than the average bond length (Fig. S22 within the Supplemental Material [63]). The difference mainly appears in the relatively average bond strength between Mn−O and Co−O bonds in the Ni-rich NMC materials. The average $-$IPCOHP values of the Co−O bond increase with the increment of Ni content but are still smaller than the Mn−O bond for all the NMC materials [Fig. 6(a)]. However, the average bond length of Co−O becomes shorter than that of Mn−O in the Ni-rich NMC materials (see Fig. S22 within the Supplemental Material [63]). Inspecting the average ICOBI in Fig. 6(c), one can find that the shorter length of the Co−O bond in Ni-rich NMC materials is mainly induced by strengthened covalent bonding, since the average ICOBI values of the Co−O bond are almost the same as that of the Mn−O bond in Ni-rich NMC materials like NMC71515 and NMC811. Nevertheless, due to the aforementioned facts that ionic bonding plays a stronger role than covalent bonding in the M−O bond of layered NMC materials [Figs. 6(c) and 6(d)] and the strong ionic bonding of Mn−O bond, the average bond strength of Co−O is still smaller than that of Mn−O, as shown by the average $-$IPCOHP values in Fig. 6(a). Therefore, the more correctly measured bond strength by $-$IPCOHP provides a better quantitative description method than the rough qualitative explanation proposed by Sun and Zhao [38], which considers only the influence of variation of the ionic size of Ni ions.

V. CONCLUSIONS

The isotropic and anisotropic elastic mechanical properties of seven layered NMC cathode materials with different compositions are systematically and comprehensively studied through first-principles calculations. The tuning relationship of Ni, Mn, and Co compositions on the isotropic and anisotropic mechanical properties of

NMC materials is investigated by contrasting their individual contributions. It is found that the elastic moduli of NMC materials decrease as the Ni content increases, and Mn plays a positive role in enhancing the elastic moduli. Besides, the applicability and correct usage of Pugh's ratio in metal-oxides like NMC materials is clarified, and the relative ductility and brittleness analysis based on Pugh's ratio and the isotropic Poisson's ratio reveals that NMC442 and NMC71515 show higher ductility due to their relatively lower elastic moduli. Analysis of the 3D spatial distribution characteristics of the anisotropic mechanical properties of NMC materials demonstrates that the distributions of directions of the extreme values of various anisotropic mechanical properties all exhibit an approximately trigonal symmetry to some extent, with at least six global maxima and six global minima distributed around the *c* axis. By investigating the elastic anisotropy within the three major crystallographic planes (families), it is found that the anisotropy is most prominent in the {2$\bar{1}$0} crystal plane family, in which the most global maxima and minima of various anisotropic mechanical properties are located. An investigation of the relationships between the distribution directions of global maximum and minimum values of Young's moduli and the atomic packing direction in the (2$\bar{1}$0) crystal plane with the most prominent anisotropy reveals that the (104) plane and [$\bar{4}$8$\bar{1}$] direction are, respectively, prone to be the cleavage plane and cleavage direction, along which microcracks and even mechanical failure may be susceptible to occur due to stress concentration. Through the examination of the overall elastic anisotropy of various NMC materials by using the custom-defined anisotropy parameters, the universal elastic anisotropy index, A^U, and the Kube's log-Euclidean elastic anisotropy index, A^L, it is found that NMC333, NMC552, and NMC811 display a relatively low elastic anisotropy compared with the others, and the role of Mn is beneficial not only for enhancing the elastic moduli but also reducing the mechanical anisotropy of NMC materials. After elaborating the physical meaning of the Cauchy pressure, its relations with Pugh's ratio and Poisson's ratio, as well as its proper use, the qualitative bonding character of layered NMC materials is evaluated by the Cauchy pressure, and the results indicate that the intralayer directional O−TM−O bonds have significant covalency, while the interlayer directional O−Li−O bonds are nearly ionic bonding dominated; these results are further proved by the quantitative ICOBI values. Finally, through quantitative chemical bond analysis by −IPCOHP and ICOBI, we highlight that the reason for the dependence of the elastic moduli of NMC materials on the TM composition lies in the difference in the TM–O bond strengths, and the positive effect of Mn on enhancing the elastic moduli of NMC materials mainly stems from the contribution of the ionic bonding part of the Mn−O bond due to the high average valence state (+4) of Mn ions. This reveals that, in addition

to the many factors that have already been reported, the improvement of the mechanical properties of NMC cathode materials may also be one of the reasons for effectively enhancing the cycling performance by doping with other high-valence-state ions.

By gaining insights into the elastic mechanical properties, this research provides a fundamental understanding of the elastic mechanical behavior in layered NMC materials. The findings presented in this study serve as a valuable resource for the subsequent further study of the microscopic processes related to elastic mechanical properties, such as crack propagations, dislocation interactions, and phase transitions, in layered NMC cathode materials. Overall, this investigation highlights the significance of considering the elastic mechanical aspects of cathode materials and may provide guidance for the design and development of advanced LIBs with improved performance, enhanced safety, and prolonged lifespan. Further investigations into the evolution of the elastic mechanical behavior of NMC materials in various delithiation states, as well as the impact of Li-Ni exchange on their elastic mechanical properties, are about to be conducted soon.

[1] W. Li, E. M. Erickson, and A. Manthiram, High-nickel layered oxide cathodes for lithium-based automotive batteries, Nat. Energy **5**, 26 (2020).

[2] S.-T. Myung, F. Maglia, K.-J. Park, C. S. Yoon, P. Lamp, S.-J. Kim, and Y.-K. Sun, Nickel-rich layered cathode materials for automotive lithium-ion batteries: Achievements and perspectives, ACS Energy Lett. **2**, 196 (2017).

[3] B. Namkoong, N. Y. Park, G. T. Park, J. Y. Shin, T. Beierling, C. S. Yoon, and Y. K. Sun, High-energy Ni-rich cathode materials for long-range and long-life electric vehicles, Adv. Energy Mater. **12**, 2200615 (2022).

[4] H.-H. Sun and A. Manthiram, Impact of microcrack generation and surface degradation on a nickel-rich layered Li[Ni$_{0.9}$Co$_{0.05}$Mn$_{0.05}$]O$_2$ cathode for lithium-ion batteries, Chem. Mater. **29**, 8486 (2017).

[5] H.-H. Ryu, K.-J. Park, C. S. Yoon, and Y.-K. Sun, Capacity fading of Ni-rich Li[Ni$_x$Co$_y$Mn$_{1-x-y}$]O$_2$ ($0.6 \leq x \leq 0.95$) cathodes for high-energy-density lithium-ion batteries: Bulk or surface degradation?, Chem. Mater. **30**, 1155 (2018).

[6] H. H. Ryu, G. T. Park, C. S. Yoon, and Y. K. Sun, Microstructural degradation of Ni-rich Li[Ni$_x$Co$_y$Mn$_{1-x-y}$]O$_2$ cathodes during accelerated calendar aging, Small **14**, e1803179 (2018).

[7] J. H. Kim, H. H. Ryu, S. J. Kim, C. S. Yoon, and Y. K. Sun, Degradation mechanism of highly Ni-rich Li[Ni$_x$Co$_y$Mn$_{1-x-y}$]O$_2$ cathodes with $x > 0.9$, ACS Appl. Mater. Interfaces **11**, 30936 (2019).

[8] T. M. M. Heenan, A. Wade, C. Tan, J. E. Parker, D. Matras, A. S. Leach, J. B. Robinson, A. Llewellyn, A. Dimitrijevic, R. Jervis, P. D. Quinn, D. J. L. Brett, and P. R. Shearing, Identifying the origins of microstructural defects such as cracking within Ni-rich NMC811 cathode particles for lithium-ion batteries, Adv. Energy Mater. **10**, 2002655 (2020).

[9] N.-Y. Park, G.-T. Park, S.-B. Kim, W. Jung, B.-C. Park, and Y.-K. Sun, Degradation mechanism of Ni-rich cathode materials: Focusing on particle interior, ACS Energy Lett. **7**, 2362 (2022).

[10] Y. Mao, X. Wang, S. Xia, K. Zhang, C. Wei, S. Bak, Z. Shadike, X. Liu, Y. Yang, R. Xu, P. Pianetta, S. Ermon, E. Stavitski, K. Zhao, Z. Xu, F. Lin, X.-Q. Yang, E. Hu, and Y. Liu, High-voltage charging-induced strain, heterogeneity, and micro-cracks in secondary particles of a nickel-rich layered cathode material, Adv. Funct. Mater. **29**, 1900247 (2019).

[11] G. Li, Z. Zhang, Z. Huang, C. Yang, Z. Zuo, and H. Zhou, Understanding the accumulated cycle capacity fade caused by the secondary particle fracture of LiNi$_{1-x-y}$Co$_x$Mn$_y$O$_2$ cathode for lithium ion batteries, J. Solid State Electrochem. **21**, 673 (2017).

[12] R. Xu, H. Sun, L. S. de Vasconcelos, and K. Zhao, Mechanical and structural degradation of LiNi$_x$Mn$_y$Co$_z$O$_2$ cathode in Li-ion batteries: An experimental study, J. Electrochem. Soc. **164**, A3333 (2017).

[13] R. Xu, L. S. de Vasconcelos, J. Shi, J. Li, and K. Zhao, Disintegration of meatball electrodes for LiNi$_x$Mn$_y$Co$_z$O$_2$ cathode materials, Exp. Mech. **58**, 549 (2018).

[14] L. Wang, B. Wu, D. Mu, X. Liu, Y. Peng, H. Xu, Q. Liu, L. Gai, and F. Wu, Single-crystal LiNi$_{0.6}$Co$_{0.2}$Mn$_{0.2}$O$_2$ as high performance cathode materials for Li-ion batteries, J. Alloys Compd. **674**, 360 (2016).

[15] Y. Bi, J. Tao, Y. Wu, L. Li, Y. Xu, E. Hu, B. Wu, J. Hu, C. Wang, J.-G. Zhang, Y. Qi, and J. Xiao, Reversible planar gliding and microcracking in a single-crystalline Ni-rich cathode, Science **370**, 1313 (2020).

[16] X. Fan, G. Hu, B. Zhang, X. Ou, J. Zhang, W. Zhao, H. Jia, L. Zou, P. Li, and Y. Yang, Crack-free single-crystalline Ni-rich layered NCM cathode enable superior cycling performance of lithium-ion batteries, Nano Energy **70**, 104450 (2020).

[17] X. Ou, T. Liu, W. Zhong, X. Fan, X. Guo, X. Huang, L. Cao, J. Hu, B. Zhang, Y. S. Chu, G. Hu, Z. Lin, M. Dahbi, J. Alami, K. Amine, C. Yang, and J. Lu, Enabling high energy lithium metal batteries via single-crystal Ni-rich cathode material co-doping strategy, Nat. Commun. **13**, 2319 (2022).

[18] J. Li, A. R. Cameron, H. Li, S. Glazier, D. Xiong, M. Chatzidakis, J. Allen, G. A. Botton, and J. R. Dahn, Comparison of single crystal and polycrystalline LiNi$_{0.5}$Mn$_{0.3}$Co$_{0.2}$O$_2$ positive electrode materials for high voltage Li-ion cells, J. Electrochem. Soc. **164**, A1534 (2017).

[19] X. Fan, Y. Liu, X. Ou, J. Zhang, B. Zhang, D. Wang, and G. Hu, Unravelling the influence of quasi single-crystalline architecture on high-voltage and thermal stability of LiNi$_{0.5}$Co$_{0.2}$Mn$_{0.3}$O$_2$ cathode for lithium-ion batteries, Chem. Eng. J. **393**, 124709 (2020).

[20] Y. Liu, J. Harlow, and J. Dahn, Microstructural observations of "single crystal" positive electrode materials before and after long term cycling by cross-section scanning electron microscopy, J. Electrochem. Soc. **167**, 020512 (2020).

[21] K. Taghikhani, P. J. Weddle, R. M. Hoffman, J. R. Berger, and R. J. Kee, Electro-chemo-mechanical finite-element model of single-crystal and polycrystalline NMC cathode particles embedded in an argyrodite solid electrolyte, Electrochim. Acta **460**, 142585 (2023).

[22] G. Qian, Y. Zhang, L. Li, R. Zhang, J. Xu, Z. Cheng, S. Xie, H. Wang, Q. Rao, Y. He, Y. Shen, L. Chen, M. Tang, and Z.-F. Ma, Single-crystal nickel-rich layered-oxide battery cathode materials: Synthesis, electrochemistry, and intra-granular fracture, Energy Storage Mater. **27**, 140 (2020).

[23] G.-M. Han, Y.-S. Kim, H.-H. Ryu, Y.-K. Sun, and C. S. Yoon, Structural stability of single-crystalline Ni-rich layered cathode upon delithiation, ACS Energy Lett. **7**, 2919 (2022).

[24] L. Ni, S. Zhang, A. Di, W. Deng, G. Zou, H. Hou, and X. Ji, Challenges and strategies towards single-crystalline Ni-rich layered cathodes, Adv. Energy Mater. **12**, 2201510 (2022).

[25] P. Yan, J. Zheng, M. Gu, J. Xiao, J.-G. Zhang, and C.-M. Wang, Intragranular cracking as a critical barrier for high-voltage usage of layer-structured cathode for lithium-ion batteries, Nat. Commun. **8**, 14101 (2017).

[26] Z. Xu, M. M. Rahman, L. Mu, Y. Liu, and F. Lin, Chemomechanical behaviors of layered cathode materials in alkali metal ion batteries, J. Mater. Chem. A **6**, 21859 (2018).

[27] P. Yan, J. Zheng, T. Chen, L. Luo, Y. Jiang, K. Wang, M. Sui, J.-G. Zhang, S. Zhang, and C. Wang, Coupling of electrochemically triggered thermal and mechanical effects to aggravate failure in a layered cathode, Nat. Commun. **9**, 2437 (2018).

[28] C. Wang, L. Han, R. Zhang, H. Cheng, L. Mu, K. Kisslinger, P. Zou, Y. Ren, P. Cao, F. Lin, and H. L. Xin, Resolving atomic-scale phase transformation and oxygen loss mechanism in ultrahigh-nickel layered cathodes for cobalt-free lithium-ion batteries, Matter **4**, 2013 (2021).

[29] C. Wang, R. Zhang, K. Kisslinger, and H. L. Xin, Atomic-scale observation of O1 faulted phase-induced deactivation of LiNiO$_2$ at high voltage, Nano Lett. **21**, 3657 (2021).

[30] M. Sadowski, L. Koch, K. Albe, and S. Sicolo, Planar gliding and vacancy condensation: The role of dislocations in the chemomechanical degradation of layered transition-metal oxides, Chem. Mater. **35**, 584 (2023).

[31] C. Wang, X. Wang, R. Zhang, T. Lei, K. Kisslinger, and H. L. Xin, Resolving complex intralayer transition motifs in high-Ni-content layered cathode materials for lithium-ion batteries, Nat. Mater. **22**, 235 (2023).

[32] C. Monroe and J. Newman, The impact of elastic deformation on deposition kinetics at lithium/polymer interfaces, J. Electrochem. Soc. **152**, A396 (2005).

[33] Z. Ahmad and V. Viswanathan, Role of anisotropy in determining stability of electrodeposition at solid-solid interfaces, Phys. Rev. Mater. **1**, 055403 (2017).

[34] K. Zeng and J. Zhu, Surface morphology, elastic modulus and hardness of thin film cathodes for Li-ion rechargeable batteries, Mech. Mater. **91**, 323 (2015).

[35] D. Kim, H. C. Shim, T. G. Yun, S. Hyun, and S. M. Han, High throughput combinatorial analysis of mechanical and electrochemical properties of Li[Ni$_x$Co$_y$Mn$_z$]O$_2$ cathode, Extreme Mech. Lett. **9**, 439 (2016).

[36] L. S. d. Vasconcelos, R. Xu, J. Li, and K. Zhao, Grid indentation analysis of mechanical properties of composite electrodes in Li-ion batteries, Extreme Mech. Lett. **9**, 495 (2016).

[37] E. J. Cheng, K. Hong, N. J. Taylor, H. Choe, J. Wolfenstine, and J. Sakamoto, Mechanical and physical properties of LiNi$_{0.33}$Mn$_{0.33}$Co$_{0.33}$O$_2$ (NMC), J. Eur. Ceram. Soc. **37**, 3213 (2017).

[38] H. Sun and K. Zhao, Electronic structure and comparative properties of LiNi$_x$Mn$_y$Co$_z$O$_2$ cathode materials, J. Phys. Chem. C **121**, 6002 (2017).

[39] Y. Qi, L. G. Hector, C. James, and K. J. Kim, Lithium concentration dependent elastic properties of battery electrode materials from first principles calculations, J. Electrochem. Soc. **161**, F3010 (2014).

[40] L. Wu and J. Zhang, *Ab initio* study of anisotropic mechanical properties of LiCoO$_2$ during lithium intercalation and deintercalation process, J. Appl. Phys. **118**, 225101 (2015).

[41] L. Bellaiche and D. Vanderbilt, Virtual crystal approximation revisited: Application to dielectric and piezoelectric properties of perovskites, Phys. Rev. B **61**, 7877 (2000).

[42] G. M. Hua and D. Y. Li, A first-principles study on the mechanical and thermodynamic properties of (Nb$_{1-x}$Ti$_x$)C complex carbides based on virtual crystal approximation, RSC Adv. **5**, 103686 (2015).

[43] S. Li, Z. Jiang, J. Han, Z. Xu, C. Wang, H. Huang, C. Yu, S.-J. Lee, P. Pianetta, H. Ohldag, J. Qiu, J.-S. Lee, F. Lin, K. Zhao, and Y. Liu, Mutual modulation between surface chemistry and bulk microstructure within secondary particles of nickel-rich layered oxides, Nat. Commun. **11**, 4433 (2020).

[44] N. Sharma, D. Meng, X. Wu, L. S. de Vasconcelos, L. Li, and K. Zhao, Nanoindentation measurements of anisotropic mechanical properties of single crystalline NMC cathodes for Li-ion batteries, Extreme Mech. Lett. **58**, 101920 (2023).

[45] G. Kresse and J. Furthmüller, Efficient iterative schemes for *ab initio* total-energy calculations using a plane-wave basis set, Phys. Rev. B **54**, 11169 (1996).

[46] G. Kresse and J. Furthmüller, Efficiency of *ab-initio* total energy calculations for metals and semiconductors using a plane-wave basis set, Comput. Mater. Sci. **6**, 15 (1996).

[47] P. Hohenberg and W. Kohn, Inhomogeneous electron gas, Phys. Rev. **136**, B864 (1964).

[48] W. Kohn and L. J. Sham, Self-consistent equations including exchange and correlation effects, Phys. Rev. **140**, A1133 (1965).

[49] J. P. Perdew, K. Burke, and M. Ernzerhof, Generalized gradient approximation made simple, Phys. Rev. Lett. **77**, 3865 (1996).

[50] J. Paier, R. Hirschl, M. Marsman, and G. Kresse, The Perdew-Burke-Ernzerhof exchange-correlation functional applied to the G2-1 test set using a plane-wave basis set, J. Chem. Phys. **122**, 234102 (2005).

[51] P. E. Blöchl, Projector augmented-wave method, Phys. Rev. B **50**, 17953 (1994).

[52] D. Hobbs, G. Kresse, and J. Hafner, Fully unconstrained noncollinear magnetism within the projector augmented-wave method, Phys. Rev. B **62**, 11556 (2000).

[53] V. V. Anisimov, J. Zaanen, and O. K. Andersen, Band theory and Mott insulators: Hubbard U instead of Stoner I, Phys. Rev. B **44**, 943 (1991).

[54] S. L. Dudarev, G. A. Botton, S. Y. Savrasov, C. J. Humphreys, and A. P. Sutton, Electron-energy-loss spectra and the structural stability of nickel oxide: An LSDA+U study, Phys. Rev. B **57**, 1505 (1998).

[55] Y. Wei, J. Zheng, S. Cui, X. Song, Y. Su, W. Deng, Z. Wu, X. Wang, W. Wang, M. Rao, Y. Lin, C. Wang, K. Amine, and F. Pan, Kinetics tuning of Li-ion diffusion in layered Li(Ni$_x$Mn$_y$Co$_z$)O$_2$, J. Am. Chem. Soc. **137**, 8364 (2015).

[56] J. Zheng, T. Liu, Z. Hu, Y. Wei, X. Song, Y. Ren, W. Wang, M. Rao, Y. Lin, Z. Chen, J. Lu, C. Wang, K. Amine, and F. Pan, Tuning of thermal stability in layered Li(Ni$_x$Mn$_y$Co$_z$)O$_2$, J. Am. Chem. Soc. **138**, 13326 (2016).

[57] M. de Jong, W. Chen, T. Angsten, A. Jain, R. Notestine, A. Gamst, M. Sluiter, C. K. Ande, S. van der Zwaag, J. J. Plata, C. Toher, S. Curtarolo, G. Ceder, K. A. Persson, and M. Asta, Charting the complete elastic properties of inorganic crystalline compounds, Sci. Data **2**, 150009 (2015).

[58] J. Zheng, G. Teng, C. Xin, Z. Zhuo, J. Liu, Q. Li, Z. Hu, M. Xu, S. Yan, W. Yang, and F. Pan, Role of superexchange interaction on tuning of Ni/Li disordering in layered Li(Ni$_x$Mn$_y$Co$_z$)O$_2$, J. Phys. Chem. Lett. **8**, 5537 (2017).

[59] B. J. Hwang, Y. W. Tsai, D. Carlier, and G. Ceder, A combined computational/experimental study on LiNi$_{1/3}$Co$_{1/3}$Mn$_{1/3}$O$_2$, Chem. Mater. **15**, 3676 (2003).

[60] N. A. Chernova, M. Ma, J. Xiao, M. S. Whittingham, J. Breger, and C. P. Grey, Layered Li$_x$Ni$_y$Mn$_y$Co$_{1-2y}$O$_2$ cathodes for lithium ion batteries: Understanding local structure via magnetic properties, Chem. Mater. **19**, 4682 (2007).

[61] H. J. Yu, Y. M. Qian, M. R. Otani, D. M. Tang, S. H. Guo, Y. B. Zhu, and H. S. Zhou, Study of the lithium/nickel ions exchange in the layered LiNi$_{0.42}$Mn$_{0.42}$Co$_{0.16}$O$_2$ cathode material for lithium ion batteries: Experimental and first-principles calculations, Energy Environ. Sci. **7**, 1068 (2014).

[62] M. Dixit, M. Kosa, O. S. Lavi, B. Markovsky, D. Aurbach, and D. T. Major, Thermodynamic and kinetic studies of LiNi$_{0.5}$Co$_{0.2}$Mn$_{0.3}$O$_2$ as a positive electrode material for Li-ion batteries using first principles, Phys. Chem. Chem. Phys. **18**, 6799 (2016).

[63] See the Supplemental Material at http://link.aps.org/supplemental/10.1103/PRXEnergy.3.013012 for more details about the construction of supercell models, the coordinate transformation of the elastic tensor, the assessment of elastic stability, and supporting tables and figures.

[64] Y. Koyama, I. Tanaka, H. Adachi, Y. Makimura, and T. Ohzuku, Crystal and electronic structures of superstructural $Li_{1-x}[Co_{1/3}Ni_{1/3}Mn_{1/3}]O_2$ ($0 \leq x \leq 1$), J. Power Sources **119–121**, 644 (2003).

[65] Y. Koyama, N. Yabuuchi, I. Tanaka, H. Adachi, and T. Ohzuku, Solid-state chemistry and electrochemistry of $LiCo_{1/3}Ni_{1/3}Mn_{1/3}O_2$ for advanced lithium-ion batteries: I. First-principles calculation on the crystal and electronic structures, J. Electrochem. Soc. **151**, A1545 (2004).

[66] L. S. Cahill, S. C. Yin, A. Samoson, I. Heinmaa, L. F. Nazar, and G. R. Goward, ^6Li NMR studies of cation disorder and transition metal ordering in $Li[Ni_{1/3}Mn_{1/3}Co_{1/3}]O_2$ using ultrafast magic angle spinning, Chem. Mater. **17**, 6560 (2005).

[67] N. Yabuuchi, Y. Koyama, N. Nakayama, and T. Ohzuku, Solid-state chemistry and electrochemistry of $LiCo_{1/3}Ni_{1/3}Mn_{1/3}O_2$ for advanced lithium-ion batteries: II. Preparation and characterization, J. Electrochem. Soc. **152**, A1434 (2005).

[68] D. Zeng, J. Cabana, J. Bréger, W.-S. Yoon, and C. P. Grey, Cation ordering in $Li[Ni_xMn_xCo_{(1-2x)}]O_2$-layered cathode materials: A nuclear magnetic resonance (NMR), pair distribution function, x-ray absorption spectroscopy, and electrochemical study, Chem. Mater. **19**, 6277 (2007).

[69] W. Karino, Order of the transition metal layer in $LiNi_{1/3}Co_{1/3}Mn_{1/3}O_2$ and stability of the crystal structure, Ionics **22**, 991 (2016).

[70] F. Schipper, M. Dixit, D. Kovacheva, M. Talianker, O. Haik, J. Grinblat, E. M. Erickson, C. Ghanty, D. T. Major, B. Markovsky, and D. Aurbacha, Stabilizing nickel-rich layered cathode materials by a high-charge cation doping strategy: Zirconium-doped $LiNi_{0.6}Co_{0.2}Mn_{0.2}O_2$, J. Mater. Chem. A **4**, 16073 (2016).

[71] M. Dixit, B. Markovsky, F. Schipper, D. Aurbach, and D. T. Major, Origin of structural degradation during cycling and low thermal stability of Ni-rich layered transition metal-based electrode materials, J. Phys. Chem. C **121**, 22628 (2017).

[72] K. J. Harris, J. M. Foster, M. Z. Tessaro, M. Jiang, X. Yang, Y. Wu, B. Protas, and G. R. Goward, Structure solution of metal-oxide Li battery cathodes from simulated annealing and lithium NMR spectroscopy, Chem. Mater. **29**, 5550 (2017).

[73] A. Chakraborty, S. Kunnikuruvan, M. Dixit, and D. T. Major, Review of computational studies of NCM cathode materials for Li-ion batteries, Isr. J. Chem. **60**, 850 (2020).

[74] A. Chakraborty, S. Kunnikuruvan, S. Kumar, B. Markovsky, D. Aurbach, M. Dixit, and D. T. Major, Layered cathode materials for lithium-ion batteries: Review of computational studies on $LiNi_{1-x-y}Co_xMn_yO_2$ and $LiNi_{1-x-y}Co_xAl_yO_2$, Chem. Mater. **32**, 915 (2020).

[75] J. F. Nye, *Physical Properties of Crystals: Their Representation by Tensors and Matrices* (Oxford University Press, New York, 1985).

[76] Y. Le Page and P. Saxe, Symmetry-general least-squares extraction of elastic data for strained materials from *ab initio* calculations of stress, Phys. Rev. B **65**, 104104 (2002).

[77] X. Wu, D. Vanderbilt, and D. R. Hamann, Systematic treatment of displacements, strains, and electric fields in density-functional perturbation theory, Phys. Rev. B **72**, 035105 (2005).

[78] S. H. Zhang and R. F. Zhang, AELAS: Automatic elastic property derivations via high-throughput first-principles computation, Comput. Phys. Commun. **220**, 403 (2017).

[79] S. Yalameha, Z. Nourbakhsh, and D. Vashaee, ElATools: A tool for analyzing anisotropic elastic properties of the 2D and 3D materials, Comput. Phys. Commun. **271**, 108195 (2022).

[80] W. Voigt, *Lehrbuch der Kristallphysik (mit Ausschluss der Kristalloptik)* (B. G. Teubner Verlag, Leipzig, 1928).

[81] A. Reuss, Berechnung der Fließgrenze von Mischkristallen auf Grund der Plastizitätsbedingung für Einkristalle, Z. Angew. Math. Mech. **9**, 49 (1929).

[82] R. Hill, The elastic behaviour of a crystalline aggregate, Proc. Phys. Soc. A **65**, 349 (1952).

[83] S. Singh, L. Lang, V. Dovale-Farelo, U. Herath, P. Tavadze, F.-X. Coudert, and A. H. Romero, MechElastic: A PYTHON library for analysis of mechanical and elastic properties of bulk and 2D materials, Comput. Phys. Commun. **267**, 108068 (2021).

[84] S. F. Pugh, XCII. Relations between the elastic moduli and the plastic properties of polycrystalline pure metals, London, Edinburgh Dublin Philos. Mag. J. Sci. **45**, 823 (1954).

[85] K. Chen, L. R. Zhao, and J. S. Tse, *Ab initio* study of elastic properties of Ir and Ir_3X compounds, J. Appl. Phys. **93**, 2414 (2003).

[86] A. V. Ponomareva, E. I. Isaev, Y. K. Vekilov, and I. A. Abrikosov, Site preference and effect of alloying on elastic properties of ternary $B2$ NiAl-based alloys, Phys. Rev. B **85**, 144117 (2012).

[87] Y. Zhang, H.-X. Chen, L. Duan, J.-B. Fan, L. Ni, and V. Ji, A comparison study of the structural and mechanical properties of cubic, tetragonal, monoclinic, and three orthorhombic phases of ZrO_2, J. Alloys Compd. **749**, 283 (2018).

[88] H. Niu, X. Q. Chen, P. Liu, W. Xing, X. Cheng, D. Li, and Y. Li, Extra-electron induced covalent strengthening and generalization of intrinsic ductile-to-brittle criterion, Sci. Rep. **2**, 718 (2012).

[89] G. N. Greaves, A. L. Greer, R. S. Lakes, and T. Rouxel, Poisson's ratio and modern materials, Nat. Mater. **10**, 823 (2011).

[90] J. Turley and G. Sines, The anisotropy of Young's modulus, shear modulus and Poisson's ratio in cubic materials, J. Phys. D: Appl. Phys. **4**, 264 (1971).

[91] Y. Li, The anisotropic behavior of Poisson's ratio, Young's modulus, and shear modulus in hexagonal materials, Phys. Status Solidi A **38**, 171 (1976).

[92] A. Marmier, Z. A. D. Lethbridge, R. I. Walton, C. W. Smith, S. C. Parker, and K. E. Evans, ELAM: A computer program for the analysis and representation of anisotropic

elastic properties, Comput. Phys. Commun. **181**, 2102 (2010).

[93] J. Nordmann, M. Aßmus, and H. Altenbach, Visualising elastic anisotropy: Theoretical background and computational implementation, Continuum Mech. Thermodyn. **30**, 689 (2018).

[94] S. I. Ranganathan and M. Ostoja-Starzewski, Universal elastic anisotropy index, Phys. Rev. Lett. **101**, 055504 (2008).

[95] C. M. Kube, Elastic anisotropy of crystals, AIP Adv. **6**, 095209 (2016).

[96] P. Mao, B. Yu, Z. Liu, F. Wang, and Y. Ju, Mechanical, electronic and thermodynamic properties of Mg_2Ca Laves phase under high pressure: A first-principles calculation, Comput. Mater. Sci. **88**, 61 (2014).

[97] S. Al-Qaisi, M. S. Abu-Jafar, G. K. Gopir, R. Ahmed, S. Bin Omran, R. Jaradat, D. Dahliah, and R. Khenata, Structural, elastic, mechanical and thermodynamic properties of terbium oxide: First-principles investigations, Results Phys. **7**, 709 (2017).

[98] Y. Medkour, F. Djeghloul, N. Bouarissa, and A. Roumili, Structural, elastic, thermodynamic, electronic, and optical properties of $CaMg_2AN_3$ ($A = $ Al and Ga): *Ab initio* investigation, Eur. Phys. J. B **94**, 88 (2021).

[99] W. Qin, S. Liu, S. Zhong, and B. Xu, Structural, mechanical, and electronic properties of Ni–Co-based layered transition metal oxide $LiNi_xCo_{1-x}O_2$ for Li-ion batteries from first principles, J. Chem. Phys. **158**, 144704 (2023).

[100] D. G. Pettifor, Theoretical predictions of structure and related properties of intermetallics, Mater. Sci. Technol. **8**, 345 (1992).

[101] C. Kuiying, L. R. Zhao, R. John, and S. T. John, Alloying effects on elastic properties of TiN-based nitrides, J. Phys. D: Appl. Phys. **36**, 2725 (2003).

[102] D. Holec, M. Friák, J. Neugebauer, and P. H. Mayrhofer, Trends in the elastic response of binary early transition metal nitrides, Phys. Rev. B **85**, 064101 (2012).

[103] G. Pagare, H. Devi, S. S. Chouhan, and S. P. Sanyal, First-principles study of electronic and elastic properties of EuCd and GdCd, Comput. Mater. Sci. **92**, 178 (2014).

[104] L. Yao, Anisotropy affects brittleness and stress-strain in ZrC, Intermetallics **148**, 107619 (2022).

[105] R. P. Thompson and W. J. Clegg, Predicting whether a material is ductile or brittle, Curr. Opin. Solid State Mater. Sci. **22**, 100 (2018).

[106] H. Ledbetter and A. Migliori, Elastic-constant systematics in f.c.c. metals, including lanthanides–actinides, Phys. Status Solidi B **245**, 44 (2008).

[107] M. W. Finnis and J. E. Sinclair, A simple empirical *N*-body potential for transition metals, Philos. Mag. A **50**, 45 (1984).

[108] R. Pasianot, D. Farkas, and E. J. Savino, Empirical many-body interatomic potential for bcc transition metals, Phys. Rev. B **43**, 6952 (1991).

[109] D. G. Pettifor and M. Aoki, Bonding and structure of intermetallics: A new bond order potential, Philos. Trans. R. Soc., A **334**, 439 (1991).

[110] S. Haussühl, Die Abweichungen von den Cauchy-Relationen, Phys. Kondens. Mater. **6**, 181 (1967).

[111] D. J. Quesnel, D. S. Rimai, and L. P. DeMejo, Elastic compliances and stiffnesses of the fcc Lennard-Jones solid, Phys. Rev. B **48**, 6795 (1993).

[112] P. Jund, R. Viennois, X. Tao, K. Niedziolka, and J.-C. Tédenac, Physical properties of thermoelectric zinc antimonide using first-principles calculations, Phys. Rev. B **85**, 224105 (2012).

[113] R. Pasianot and E. J. Savino, Embedded-atom-method interatomic potentials for hcp metals, Phys. Rev. B **45**, 12704 (1992).

[114] D. Farkas, C. Vailhe, and J. Panova, Empirical angular-dependent potentials for intermetallics, J. Phase Equilib. **18**, 530 (1997).

[115] D. Nguyen-Manh, D. G. Pettifor, S. Znam, and V. Vitek, Negative Cauchy pressure within the tight-binding approximation, MRS Online Proc. Libr. **491**, 353 (1997).

[116] A. Girshick, A. M. Bratkovsky, D. G. Pettifor, and V. Vitek, Atomistic simulation of titanium. I. A bond-order potential, Philos. Mag. A **77**, 981 (1998).

[117] D. Nguyen-Manh, D. G. Pettifor, D. J. H. Cockayne, M. Mrovec, S. Znam, and V. Vitek, Environmentally dependent bond-order potentials: New developments and applications, Bull. Mater. Sci. **26**, 43 (2003).

[118] D. Qu, C. Li, L. Bao, Z. Kong, and Y. Duan, Structural, electronic, and elastic properties of orthorhombic, hexagonal, and cubic Cu_3Sn intermetallic compounds in Sn–Cu lead-free solder, J. Phys. Chem. Solids **138**, 109253 (2020).

[119] L. Bao, D. Qu, Z. Kong, and Y. Duan, Anisotropies in elastic properties and thermal conductivities of trigonal TM_2C (TM = V, Nb, Ta) carbides, Solid State Sci. **98**, 106027 (2019).

[120] Y. Duan, Y. Wang, M. Peng, and K. Wang, Insight into anisotropies in mechanical and thermal properties of $AGdS_2$ ($A = $ alkali metals) ternary gadolinium sulfides, Mater. Today Commun. **26**, 101991 (2021).

[121] D. Farkas, Interatomic potentials for Ti-Al with and without angular forces, Modell. Simul. Mater. Sci. Eng. **2**, 975 (1994).

[122] M. Peng, H. Shou, and Y. Cao, First-principles calculations of structural, elastic and thermodynamic properties of (h, r)-$TiAl_2$, Phys. B **561**, 29 (2019).

[123] S. Ganeshan, S. L. Shang, H. Zhang, Y. Wang, M. Mantina, and Z. K. Liu, Elastic constants of binary Mg compounds from first-principles calculations, Intermetallics **17**, 313 (2009).

[124] W.-H. Chen, C.-F. Yu, K.-N. Chiang, and H.-C. Cheng, First-principles density functional calculations of physical properties of orthorhombic Au_2Al crystal, Intermetallics **62**, 60 (2015).

[125] E. Deligoz and H. Ozisik, Mechanical and dynamical stability of TiAsTe compound from *ab initio* calculations, Philos. Mag. **95**, 2294 (2015).

[126] B. Liu, X.-J. Wang, and X.-Y. Bu, First principles investigations of structural, electronic and elastic properties of ammonium perchlorate under high pressures, Acta Phys. Sin. **65**, 126102 (2016).

[127] S. Ahmad, R. Ahmad, S. Jalali-Asadabadi, Z. Ali, and I. Ahmad, First principle studies of structural, magnetic and elastic properties of orthorhombic rare-earth diaurides intermetallics RAu$_2$ (R = La, Ce, Pr and Eu), Mater. Chem. Phys. **212**, 44 (2018).

[128] S. Al, M. Yortanlı, and E. Mete, Lithium metal hydrides (Li$_2$CaH$_4$ and Li$_2$SrH$_4$) for hydrogen storage; mechanical, electronic and optical properties, Int. J. Hydrogen Energy **45**, 18782 (2020).

[129] K. Momma and F. Izumi, VESTA 3 for three-dimensional visualization of crystal, volumetric and morphology data, J. Appl. Cryst. **44**, 1272 (2011).

[130] Y.-K. Sun, S.-T. Myung, M.-H. Kim, J. Prakash, and K. Amine, Synthesis and characterization of Li[(Ni$_{0.8}$Co$_{0.1}$Mn$_{0.1}$)$_{0.8}$(Ni$_{0.5}$Mn$_{0.5}$)$_{0.2}$]O$_2$ with the microscale core−shell structure as the positive electrode material for lithium batteries, J. Am. Chem. Soc. **127**, 13411 (2005).

[131] R. Golesorkhtabar, P. Pavone, J. Spitaler, P. Puschnig, and C. Draxl, ElaStic: A tool for calculating second-order elastic constants from first principles, Comput. Phys. Commun. **184**, 1861 (2013).

[132] C. M. Kube and M. de Jong, Elastic constants of polycrystals with generally anisotropic crystals, J. Appl. Phys. **120**, 165105 (2016).

[133] F. Mouhat and F.-X. Coudert, Necessary and sufficient elastic stability conditions in various crystal systems, Phys. Rev. B **90**, 224104 (2014).

[134] M. Born, On the stability of crystal lattices. I, Math. Proc. Cambridge Philos. Soc. **36**, 160 (1940).

[135] M. Born and K. Huang, *Dynamical Theory of Crystal Lattices* (Oxford University Press, Oxford, 1954).

[136] G. Grimvall, B. Magyari-Köpe, V. Ozoliņš, and K. A. Persson, Lattice instabilities in metallic elements, Rev. Mod. Phys. **84**, 945 (2012).

[137] V. Wang, N. Xu, J.-C. Liu, G. Tang, and W.-T. Geng, VASP-KIT: A user-friendly interface facilitating high-throughput computing and analysis using VASP code, Comput. Phys. Commun. **267**, 108033 (2021).

[138] R. Gaillac, P. Pullumbi, and F. X. Coudert, ELATE: An open-source online application for analysis and visualization of elastic tensors, J. Phys.: Condens. Matter **28**, 275201 (2016).

[139] K. E. Evans, M. A. Nkansah, I. J. Hutchinson, and S. C. Rogers, Molecular network design, Nature **353**, 124 (1991).

[140] R. H. Baughman, J. M. Shacklette, A. A. Zakhidov, and S. Stafström, Negative Poisson's ratios as a common feature of cubic metals, Nature **392**, 362 (1998).

[141] L. J. Hall, V. R. Coluci, D. S. Galvão, M. E. Kozlov, M. Zhang, S. O. Dantas, and R. H. Baughman, Sign change of Poisson's ratio for carbon nanotube sheets, Science **320**, 504 (2008).

[142] V. H. Carneiro, J. Meireles, and H. Puga, Auxetic materials — a review, Mater. Sci.-Pol. **31**, 561 (2013).

[143] R. Qin, J. Zheng, and W. Zhu, Sign-tunable Poisson's ratio in semi-fluorinated graphene, Nanoscale **9**, 128 (2017).

[144] R. Lakes, Foam structures with a negative Poisson's ratio, Science **235**, 1038 (1987).

[145] A. Ulvestad, A. Singer, J. N. Clark, H. M. Cho, J. W. Kim, R. Harder, J. Maser, Y. S. Meng, and O. G. Shpyrko, Topological defect dynamics *in operando* battery nanoparticles, Science **348**, 1344 (2015).

[146] V. P. Mikhal'chenko, On the born relation for crystals with diamond and sphalerite structure, Phys. Solid State **45**, 453 (2003).

[147] M. G. Brik, First-principles calculations of electronic, optical and elastic properties of ZnAl$_2$S$_4$ and ZnGa$_2$O$_4$, J. Phys. Chem. Solids **71**, 1435 (2010).

[148] M. Jamal, S. Jalali Asadabadi, I. Ahmad, and H. A. Rahnamaye Aliabad, Elastic constants of cubic crystals, Comput. Mater. Sci. **95**, 592 (2014).

[149] M. A. Faridi, S. Tariq, M. Imran Jamil, A. Batool, S. Nadeem, and A. Amin, Pressure induced band-gap tuning in KNbO$_3$ for piezoelectric applications: Quantum DFT-GGA approach, Chin. J. Physiol. **56**, 1481 (2018).

[150] M. I. Baskes, Application of the embedded-atom method to covalent materials: A semiempirical potential for silicon, Phys. Rev. Lett. **59**, 2666 (1987).

[151] M. I. Baskes, J. S. Nelson, and A. F. Wright, Semiempirical modified embedded-atom potentials for silicon and germanium, Phys. Rev. B **40**, 6085 (1989).

[152] J. Haines, J. M. Léger, and G. Bocquillon, Synthesis and design of superhard materials, Annu. Rev. Mater. Res. **31**, 1 (2001).

[153] P. Ravindran, L. Fast, P. A. Korzhavyi, B. Johansson, J. Wills, and O. Eriksson, Density functional theory for calculation of elastic properties of orthorhombic crystals: Application to TiSi$_2$, J. Appl. Phys. **84**, 4891 (1998).

[154] R. A. Bartels and P. R. Son, The elastic Cauchy relation and ionicity, J. Phys. Chem. Solids **33**, 749 (1972).

[155] R. E. MacFarlane, J. A. Rayne, and C. K. Jones, Temperature dependence of elastic moduli of iridium, Phys. Lett. **20**, 234 (1966).

[156] O. Y. Kontsevoi, Y. N. Gornostyrev, and A. J. Freeman, Modeling the dislocation properties and mechanical behavior of Ir, Rh, and their refractory alloys, JOM **57**, 43 (2005).

[157] M. J. Cawkwell, D. Nguyen-Manh, D. G. Pettifor, and V. Vitek, Construction, assessment, and application of a bond-order potential for iridium, Phys. Rev. B **73**, 064104 (2006).

[158] D. Maurer, R. Heichele, N. Lingg, V. Müller, and K. H. Rieder, Elastic properties of purified single-crystalline rhodium, Phys. Status Solidi A **160**, 403 (1997).

[159] R. Dronskowski and P. E. Bloechl, Crystal orbital Hamilton populations (COHP): Energy-resolved visualization of chemical bonding in solids based on density-functional calculations, J. Phys. Chem. **97**, 8617 (1993).

[160] V. L. Deringer, A. L. Tchougréeff, and R. Dronskowski, Crystal orbital Hamilton population (COHP) analysis as projected from plane-wave basis sets, J. Phys. Chem. A **115**, 5461 (2011).

[161] S. Maintz, V. L. Deringer, A. L. Tchougreeff, and R. Dronskowski, Analytic projection from plane-wave and PAW wavefunctions and application to chemical-bonding analysis in solids, J. Comput. Chem. **34**, 2557 (2013).

[162] P. C. Müller, C. Ertural, J. Hempelmann, and R. Dronskowski, Crystal orbital bond index: Covalent bond orders in solids, J. Phys. Chem. C **125**, 7959 (2021).

[163] S. Maintz, V. L. Deringer, A. L. Tchougréeff, and R. Dronskowski, LOBSTER: A tool to extract chemical bonding

from plane-wave based DFT, J. Comput. Chem. **37**, 1030 (2016).

[164] R. Nelson, C. Ertural, J. George, V. L. Deringer, G. Hautier, and R. Dronskowski, LOBSTER: Local orbital projections, atomic charges, and chemical-bonding analysis from projector-augmented-wave-based density-functional theory, J. Comput. Chem. **41**, 1931 (2020).

[165] F. Xin, H. Zhou, Y. Zong, M. Zuba, Y. Chen, N. A. Chernova, J. Bai, B. Pei, A. Goel, J. Rana, F. Wang, K. An, L. F. J. Piper, G. Zhou, and M. S. Whittingham, What is the role of Nb in nickel-rich layered oxide cathodes for lithium-ion batteries?, ACS Energy Lett. **6**, 1377 (2021).

[166] G.-T. Park, B. Namkoong, S.-B. Kim, J. Liu, C. S. Yoon, and Y.-K. Sun, Introducing high-valence elements into cobalt-free layered cathodes for practical lithium-ion batteries, Nat. Energy **7**, 946 (2022).

[167] R. Zhang, C. Wang, P. Zou, R. Lin, L. Ma, L. Yin, T. Li, W. Xu, H. Jia, Q. Li, S. Sainio, K. Kisslinger, S. E. Trask, S. N. Ehrlich, Y. Yang, A. M. Kiss, M. Ge, B. J. Polzin, S. Jun Lee, W. Xu, Y. Ren, and H. L. Xin, Compositionally complex doping for zero-strain zero-cobalt layered cathodes, Nature **610**, 67 (2022).

[168] R. Zhang, C. Wang, P. Zou, R. Lin, L. Ma, T. Li, I.-h. Hwang, W. Xu, C. Sun, S. Trask, and H. L. Xin, Long-life lithium-ion batteries realized by low-Ni, Co-free cathode chemistry, Nat. Energy **8**, 695 (2023).

[169] U.-H. Kim, G.-T. Park, B.-K. Son, G. W. Nam, J. Liu, L.-Y. Kuo, P. Kaghazchi, C. S. Yoon, and Y.-K. Sun, Heuristic solution for achieving long-term cycle stability for Ni-rich layered cathodes at full depth of discharge, Nat. Energy **5**, 860 (2020).

[170] H. H. Sun, U.-H. Kim, J.-H. Park, S.-W. Park, D.-H. Seo, A. Heller, C. B. Mullins, C. S. Yoon, and Y.-K. Sun, Transition metal-doped Ni-rich layered cathode materials for durable Li-ion batteries, Nat. Commun. **12**, 6552 (2021).